Memory CD4 T cells orchestrate neoadjuvant-responsive niches in colorectal cancer liver metastases

Mayoux, Maud[1]; Litscher, Gioana[1 #]; Wiesmann, Fabius[2 #]; Vermeer, Marijne[1 #]; Jorba-Adolff, Pau[1]; Guido Vinzoni, Elena[3]; Nunez, Nicolas[4]; Sparano, Colin[1]; Vetter, Viola Katharina[2]; Friebel, Ekaterina[5]; Wertheimer, Tobias[6]; Ficht, Xenia[3]; Burr, Samira[1]; Karimi, Ariana[1]; Dergun, Stanislav[7] Schmid, Jonas[1]; Krishnarajah, Sinduya[8]; Mair, Florian[9]; Moor, Andreas[3]; Becher, Burkhard[1]; Sobottka, Bettina[2# **]; Tugues, Sònia[1,10# *]

[1] Institute of experimental immunology, University of Zurich, Switzerland; [2] Department of Pathology and Molecular Pathology, University Hospital Zurich, Switzerland; [3] Department of Biosystems Science and Engineering, ETH Zurich, 4056 Basel, Switzerland; [4] Universidad Nacional de Córdoba, Argentina; [5] Charite universitats medizin Berlin, Germany; [6] University of Freiburg, Germany; [7] Ludwig Cancer Research, Department of oncology, University of Lausanne, Switzerland; [8] Roche Pharma Research and Early Development, Roche Innovation Center Basel, Switzerland [9] ETH Zurich, Institute of Molecular Health Sciences, Switzerland; [10] Department of Immunology, Medical Faculty Mannheim, Mannheim Institute for Innate Immunosciences (MI3), Heidelberg University, Heidelberg, Germany. [#]Equal contribution.

*Correspondence: tugues@immunology.uzh.ch
**Correspondence: AnnaBettina.Sobottka-Brillout@usz.ch

Summary

Colorectal cancer frequently progresses to liver metastases (CRLM), a stage with poor prognosis. Surgical resection offers the best chance of cure, but most patients are initially ineligible. Neoadjuvant therapy can enable resection, yet response rates remain low, and mechanisms are unclear. To uncover markers associated with treatment efficacy, we profiled T cell states and their spatial organization in CRLM. We reveal distinct immune architectures, with the tumor center enriched in exhausted, regulatory, and memory T cells, but depleted of cytotoxic subsets. Responders feature CD4-coordinated niches with activated Th1-like CD4 memory T cells, stem-like and effector CD8 T cells, and spatially organized antigen-presenting cells. In contrast, non-responders harbor disorganized, myeloid-rich niches with less activated CD4 memory T cells and abundant regulatory T cells. These findings highlight activated CD4 memory T cells and their spatial niches as key markers of neoadjuvant response, offering a framework for biomarker discovery and rational immunotherapy design.

Keywords: Colorectal liver metastases, neoadjuvant therapy response, tumor immune microenvironment, spatial T cell niches, CD4 memory T cells, Th1-like helper T cells.

Introduction

Colorectal cancer (CRC) poses a major global health burden, with over 1.9 million new cases and 935,000 deaths annually [1]. The vast majority are microsatellite stable (MSS) tumors, reflecting an intact mismatch repair machinery. As a result, these tumors carry substantially fewer mutation and respond poorly to immunotherapy, including immune checkpoint blockade [2]. The liver is the most common site of metastasis in CRC, with metastases present in approximately 20% of patients at diagnosis and developing in up to 50% over the course of the disease [3]. CRLM is associated with poor outcomes, driven in part by liver-specific mechanisms of immune tolerance [4–6]. Because few patients present with resectable disease, neoadjuvant therapy is used to downstage the tumor and enable surgery. This approach combines chemotherapy, primarily fluoropyrimidine-based combinations with oxaliplatin and/or irinotecan such as FOLFOX, FOLFIRI, and the triplet FOLFOXIRI, with or without targeted agents (anti-VEGF and anti-EGFR), selected based on patient performance status and tumor mutational profile [3]. Despite these interventions, pathological responses are achieved in only a minority of patients [3,7], which is associated with improved long-term prognosis [8–11], underscoring the urgent need to understand why most fail to respond.

Immune cell infiltration strongly influences CRLM outcomes [12–16]. Both CD8 and CD4 T cells are key orchestrators of anti-tumor immunity, with their activation and differentiation states shaping both tumor progression and response to immunotherapy [17,18]. Effector and memory CD8 T cells, including resident subsets, mediate cytotoxicity and long-term immune surveillance, and consistently correlate with favorable prognosis [19–21]. CD4 T cells support anti-tumor immunity by licensing antigen-presenting cells (APCs) for CD8 T cell priming, reprogramming myeloid cells, and maintaining effector and memory T cell pools, thereby enhancing responses to checkpoint blockade [22,23]. However, in MSS CRC, low neoantigen burden impairs effective antigen presentation and cross-priming, leading to weak CD8 T cell responses and poor T cell infiltration [24–28]. In CRLM, this is exacerbated by the accumulation of dysfunctional CD8 T cells and immunosuppressive myeloid cells, contributing to an inhibitory immune microenvironment associated with poor outcomes [29,30]. Chemotherapy agents used in neoadjuvant treatment for CRLM, such as oxaliplatin and 5-fluorouracil, can trigger immunogenic cell death and remodel the immune landscape, potentially unlocking anti-tumor immunity [31–33]. Given that immune infiltration correlates with survival [12–16], resistance to therapy may stem from inadequate immune recruitment, impaired effector differentiation, or the dominance of suppressive populations. However, how treatment response to chemotherapy is affected by the composition, dynamics, and functional states of CD4 and CD8 T cells in CRLM, remains unclear.

To address this gap, we investigated how T cell states and spatial organization relate to neoadjuvant therapy response in CRLM. Using high-dimensional single-cell and spatial profiling, we mapped lymphocytes across the tumor center, invasive margin,

and adjacent perilesional normal liver. The tumor center was depleted of cytotoxic and innate lymphocytes but enriched in CD4 T cells, comprising nearly half of intratumoral lymphocytes. Responders, defined by pathological response in tumor regression grading (TRG) [8], displayed coordinated immune niches with activated Th1-like memory CD4 T cells, stem-like and effector memory CD8 T cells, and specialized APCs, suggesting a supportive pro-immunogenic microenvironment. Non-responders lacked these spatial arrangements and instead harbored regulatory and less activated memory CD4 T cells within myeloid-rich, poorly interactive niches. These spatially organized lymphocyte networks, centered on memory CD4 T cells, emerge as key markers of treatment efficacy in CRLM, informing prognosis and precision immunotherapy.

Results

CD4 T cell dominance and cytotoxic cell exclusion characterize the CRLM microenvironment

We performed high-throughput phenotyping on 76 matched samples obtained from the tumor center, invasive margin, and perilesional normal tissue of 30 patients with MSS CRLM. Most patients (28/30) had received neoadjuvant chemotherapy, with or without targeted therapy, prior to surgical resection. Histopathological response data, assessed by TRG, were available for most cases (25/30), enabling correlation between immune profiles and treatment outcomes (Figure 1A and 1B; Figure S1A). High-dimensional flow cytometry revealed a pronounced exclusion of innate-like lymphocytes (NK and γδ T cells) from the tumor center, along with a slight decrease in CD8 T cells and MAIT cells (Figures 1C-1E, Figure S1B and S1C). Conversely, CD4 T cells and regulatory T cells (Tregs) were enriched in the invasive margin and, particularly, in the tumor center, where CD4 T cells accounted for nearly 50% of tumor-infiltrating lymphocytes (Figures 1C-1E). B cells were scarce across all regions and decreased in the tumor center (Figure S1D). These changes in the lymphocyte composition were consistently observed across all samples (Figure S1E). Compared to the perilesional normal tissue and the invasive margin, lymphocytes in the tumor center exhibited increased memory and tissue residency/activation features (CD69, CD45RO), and reduced effector markers (Granzyme B (GzmB), CX3CR1, KLRG1), consistent with adaptation to a suppressive microenvironment (Figure 1F and Figure S1F). Notably, the invasive margin was enriched in T cells with progenitor-like features, marked by high TCF1 and Eomes expression, suggesting local heterogeneity in T cell differentiation states [34,35] (Figures S1F and S1G). Thus, CRLM tumors display a shift towards a CD4-dominated, non-cytotoxic immune landscape enriched for memory and residency traits.

The tumor center is enriched in memory, exhausted, and suppressive T cells

Unsupervised FlowSOM clustering identified diverse memory, effector, exhausted, and Treg subsets among CD4 and CD8 T cells (Figures 2A-2F). Within CD4 T cells,

we detected three predominant memory clusters: Mem1 and Mem2, characterized by distinct levels of CD69 and TCF1 expression, and Mem CD161, expressing CD161 and CXCR6 (Figures 2B and 2C, Figures S2A and S2B). Similarly, the CD8 T cell compartment featured a CD127^{+} memory population (Mem) and a CD69^{+} CD103^{+} resident memory (RM) subset, as well as three effector subsets expressing variable levels of CD69, GZMB and PD-1 including effector-memory cells (EM), short-lived effector cells (SLEC) and terminally differentiated effector cells (TEMRAs) (Figures 2E and 2F, Figures S3A and S3B). We also identified two exhausted CD8 T cell populations: transitory exhausted (Tex transitory) and terminally exhausted (Tex Term) (Figure 2D, Figures S3B) and two exhausted CD4 T cells populations: precursor of exhausted cells (Tpex) and proliferative exhausted cells (Tex prolif) (Figure 2B, Figures S2B).

To interrogate the immune microenvironment beyond individual cell types, we examined co-distribution patterns of lymphocyte subsets across tumor regions and samples. Hierarchical clustering of these patterns identified three distinct cellular modules (Modules 1-3) (Figure 2G) each comprising subsets whose abundance covaried across regions. Module analysis and Principal Component Analysis (PCA) revealed that the tumor center was primarily associated with memory CD4 and CD8 T cells, Tregs and exhausted T cell populations (Module 1), whereas cytotoxic effector and innate-like lymphocytes (Module 3) were excluded (Figures 2H, Figures S4A-S4D). An additional PCA based on functional marker expression further distinguished the three regions (Figure S4E), highlighting enrichment of memory and tissue residency features and diminished effector markers across lymphoid subsets in the tumor center (Figure S4F). Terminally exhausted CD8 T cells and Tregs in the tumor center displayed elevated activation and exhaustion markers (Figure S4F). Collectively, these findings uncover a spatially organized lymphocyte distribution in CRLM, with the tumor center enriched in memory CD4 and CD8 T cells, exhausted T cells, and Tregs, while the invasive margin shares features with the tumor center and perilesional normal tissue with more pronounced stem-like T cell characteristics (Figure 2I).

Distinct CD4 and CD8 T cell modules correlate with neoadjuvant treatment response

To investigate how T cell states relate to neoadjuvant therapy, we stratified patients based on histopathological regression using TRG, a histopathological measure that evaluates tumor shrinkage after therapy and correlates with long-term outcomes [8,9]. Patients were grouped as responders (R, TRG 1 & 2), partial responders (PR, TRG 3), and non-responders (NR, TRG 4 & 5) (Figure S5A). We analyzed co-distribution patterns of lymphocytes specifically within the tumor center, identifying distinct treatment-associated immune metastatic modules (Met 1-5) (Figure 3A), whose abundances varied together. Responders were enriched in Met 4, characterized by a CD4 T cell memory subset (Mem2), CD8 Mem and EM T cells; while non-responders were more represented with module Met 3, characterized by a different subset of CD4 memory T cells (Mem1), Tregs and CD8 innate-like cells (Figures 3B-3D, Figure S5B).

PCA analysis of immune subset frequencies in the tumor center further separated responders from non-responders, mirroring the associations with the populations identified in the module analysis, and additionally highlighting CD8 RM cells as correlated with treatment response (Figures 3E and 3F). A similar pattern was observed at the invasive margin, mainly driven by CD8 T cells, whereas immune profiles of the perilesional normal tissue did not clearly differ by response status (Figure S5C and S5D). Manual gating confirmed a strong association between CD4 Mem2 cells in the tumor center and treatment response (R = -0.694) (Figure S6A - S6C). Notably, the increase of CD4 Mem2 cells in the tumor center was accompanied by a reduction in CD4 Mem1 cells (Figure S6D), suggesting that CD4 Mem2 cells are preferentially activated or more capable of persisting and infiltrating this region. Together, our findings identify a treatment-associated lymphoid signature in CRLM, marked by the expansion of a specific CD4 memory subset (Mem2) along with increased CD8 Mem, EM and RM T cells, accompanied by a concurrent reduction in Tregs and a distinct CD4 memory population (Mem1) (Figure 3G).

Responder-associated T cells display Th1-like CD4 and CD8 progenitor signatures

The distinct associations of CD4 and CD8 T cell subsets with neoadjuvant therapy response prompted us to further investigate their roles within the tumor microenvironment. Using the BD Rhapsody platform [36], we profiled samples from eight MSS CRLM patients (Figure S7A), six of which were newly collected, through combined single-cell transcriptomic, proteomic and TCR sequencing. This integrative approach enabled identification of the CD4 and CD8 T cell subsets described above (Figure 4A-4D, Figure S7B-S7D, Figure 2). The distribution of these subsets across regions was consistent with the flow cytometry results (Figures S7E and S7F). CD4 Mem2 cells, enriched in responders and identified at the protein level by high CD127 and CD69, and low expression of CD161 (Figure 4B), displayed transcriptomic features of activation and differentiation, including expression of Th1-associated genes such as *CD40L*, *TNF* and *IFNG* (Figure 4E and 4F; Figure S7C and S7G). Complementary gene regulatory networks analysis with SCENIC [37] confirmed activation of key regulons (*STAT1*, *IRF2/3/5*, and *ETS1*), supporting a Th1-like transcriptional program in these cells (Figure S7H). Conversely, CD4 Mem1 cells, predominating in non-responders, retained stem-like and circulating features marked by *TCF7* and *CCR7* (Figure 4E and 4F), consistent with the low expression of the activation and residency marker [38] CD69 (Figure 4B). These cells expressed genes linked to nuclear factor κB (NF-κB) signaling (Figure 4E) and elevated NF-κB and AP-1 regulon activity (Figure S7H), suggesting a stem-like state with activation potential. CD4 Mem1 cells shared transcriptional programs overlapping with CD4 Mem CD161, including hypoxia- and TGF-β–related pathways (Figure 4F; Figure S7C and S7G). However, the CD4 Mem CD161, which was not linked to response (Figure 3), showed a more distinct Th17-like signature (Figure 4F, Figure S7G). Finally, Tregs exhibited high CD25 protein levels and elevated expression of *CCR8* and *IL1R1*, markers

220 indicative of activated, immunosuppressive phenotype[39,40], consistent with their preferential enrichment in non-responders (Figure 4B, Figure S7C).

Parallel to the distinct CD4 profiles, CD8 T cells associated with response to neoadjuvant treatment spanned a continuum from stem-like memory to effector and
225 tissue resident states. Mem CD8 T cells displayed a stem-like profile, marked by high expression of *TCF7* and *IL7R*, along with features of circulating cells and low clonal expansion, as assessed by TCR sequencing (Figures 4G and 4H, Figure S7I). In contrast, EM CD8 T cells expressed effector-associated genes such as *EOMES* and *GZMK,* co-stimulatory molecules *CD28* and *SLAMF6*, and the activation markers
230 CD69 and KLRG1, detected by protein analysis (Figure 4D and 4G). Moderate expression of *TOX* and *TCF7* with emerging cytotoxicity signatures suggests a balance between activation and progenitor of exhausted cells [17] (Figures 4G and 4H). Additionally, EM CD8 T cells showed some clonal expansion and shared TCRs with CD8 Mem, RM, SLEC and TEMRA subsets, suggesting multipotent differentiation
235 potential between stem-like memory and more differentiated cytotoxic subsets (Figure S7I and S7J). CD8 RM cells, also linked to response, expressed tissue residency markers and signs of mild dysfunction (Figure 4G and 4H). In contrast, Tex Term CD8 T cells displayed high surface levels of TIM-3 and PD-1, along with elevated *ENTPD1* (coding for CD39) and *TOX* transcripts (Figure 4D and 4G). Although these cells
240 showed extensive clonal expansion and TCR sharing, they were not associated with response (Figure S7I and S7J, Figure 3). Together, these data suggests that effective anti-tumor activity after neoadjuvant therapy is marked by coordinated local T cell activation, involving Th1-like CD4 memory helpers and a spectrum of CD8 subsets with ongoing clonal expansion including stem-like memory, effector memory, and
245 tumor-reactive tissue-resident cells.

CD4 Mem2 T cells show enhanced Th1 activity, while CD8 memory subsets display complementary functions

250 Given the association of CD4 Mem2 and CD8 memory and effector subsets with response to neoadjuvant therapy, we sought to validate their functional properties. We performed *ex vivo* stimulation assays of sorted T cell subsets from the invasive margin and the tumor center of 13 patients using suboptimal stimulation with a CD3 agonist combined with recombinant CD40 protein or a CD28 agonist (Figures 5A, Figure S8A-
255 S8D). This approach confirmed the functional polarization inferred from the transcriptomic data. CD4 Mem2 cells, enriched in responders, exhibited enhanced Th1-like activation, demonstrated by higher levels of T-bet, CD40L and PD-1 compared to CD4 Mem1 cells (Figures 5B and 5C). They also produced more IFN-γ and TNF upon aCD3/CD40 stimulation and outperformed CD4 Mem1 in IL-2
260 production in response to aCD3/aCD28 (Figure 5D), consistent with a robust helper function. In line with their transcriptomic and proteomic profile, CD8 EM cells showed an effector-ready phenotype with elevated expression of activation markers (Figure 5E and 5F), yet produced lower levels of cytokines such as IL-2, IFN-γ and TNF upon stimulation compared to Mem CD8 T cells (Figure 5D). In contrast, Mem CD8 cells,

265 which display stem-like features, maintained robust cytokine production (Figure 5D), suggesting preserved functionality and a potential role as a reservoir for replenishing effector CD8 subsets. Together, these findings support a model in which effective anti-tumor immunity is sustained through complementary roles: CD4 Mem2 cells provide helper functions through cytokine production and CD40L expression; CD8 Mem cells
270 serve as a responsive memory pool; and CD8 EM cells deliver immediate effector responses.

Integrated single-cell analysis reveals conserved and treatment-adapted T cells in CRLM

275

To evaluate the generalizability and treatment specificity of the T cell states identified in our cohort, we next examined whether these subsets were also present in treatment-naive CRLM. We analyzed a publicly available scRNAseq dataset from 10 untreated CRLM patients, encompassing perilesional normal tissue and tumor center
280 samples [29]. Integrating our dataset with the public scRNA-seq data using Harmony [41] revealed shared CD4 T cell subsets across both cohorts (Figure S9A), displaying gene signatures closely matching those defined by our Rhapsody analysis (Figure S9B, see Methods for details). Notably, the tumor center of untreated patients showed an expansion of CD4 Mem1 cells, which exhibit a more stem-like and less activated
285 profile, and reduced abundance of activated CD4 Mem2 (Figure S9C), suggesting that neoadjuvant therapy may promote their differentiation towards Th1-like helper cells. In contrast, the CD8 T cell compartment diverged substantially between untreated and treated patients, particularly within effector memory populations (Figure S9D-S9F), indicating a stronger impact of chemotherapy on CD8 T cell states, consistent with
290 previous observations [42].

Analysis of an independent dataset of neoadjuvant-treated patients [43], stratified by treatment response, identified a CD4 memory population (Cluster 1) characterized by high *IL7R*, *CD69* and *CD40LG* and low *KLRB1* (encoding CD161) expression,
295 resembling the CD4 Mem2 subset (Figure S9G and S9H). This cluster exhibited a Th1-like profile and was enriched in treated patients with partial response (treated-PR, n=3) compared to those with progressive or stable disease (treated-PD/SD, n=6) or untreated patients (n=11) (Figure S9I and S9J). Together, these findings reinforce the association between local Th1 polarization of memory CD4 T cells and favorable
300 therapeutic outcomes.

Spatial coordination of CD4 memory, CD8 T cells, and APCs defines treatment-responsive niches

305 Given the association of memory Th1-like CD4 and stem-like CD8 T cells with neoadjuvant therapy response in CRLM, we investigated their spatial relationship with APCs, which are critical for sustaining stem-like CD8 T cell populations and orchestrating effective anti-tumor immunity [44–47]. To this end, we performed high-dimensional spatial profiling using sequential Immunofluorescence on the COMET

platform (Lunaphore) [48] on tissue microarrays from 30 MSS CRLM patients (Figure 6A, Figure S1A). Unsupervised clustering identified the major populations of tumor, lymphoid, and myeloid cells (Figure S10A and S10B) and revealed immune cell enrichment at the invasive margin, predominantly CD4 T cells and myeloid cells, followed by CD8 T cells (Figure S10C). The tumor center exhibited lower overall infiltration but was enriched in CD4 T cells and Tregs (Figure S10C). Responders showed higher CD4 and CD8 T cell densities in both regions (Figure S10D), reinforcing the link between T cell infiltration and effective anti-tumor responses [12–16].

To resolve T cell states, we subclustered CD4 and CD8 T cell populations based on TCF1, CD69, and GzmK expression (Figure S10E–H). CD4 T cells spanned a continuum from TCF1^{+} CD69^{-} (Mem1-like), through early TCF1^{+} CD69^{+} (Mem2-like), to more differentiated TCF1^{-} CD69^{+} states (Figure S10E and S10F). CD8 subsets featured TCF1^{+} stem-like (e.g. CD8 Mem) and GzmK^{+} EM cells, both previously associated with treatment response (Figure S10G and S10H). We also identified CD4 and CD8 Tex Term and CD4 Tpex (Figure S10E-H). Myeloid populations included two CD68^{+} HLA-DR^{+} macrophage subsets distinguished by CD11c levels; DCs (CD11c^{+} HLA-DR^{+} CD68^{-}); and CD11b^{+} HLA-DR$^{+/-}$ myeloid cells lacking CD68 (Figure S10I and S10J). At the invasive margin, we observed an enrichment of CD4 Mem2-like cells, TCF1^{+} stem-like CD8 and GzmK^{+} EM CD8 T cells (Figure S10K), suggesting active local T cell priming and differentiation. Responders exhibited increased densities of early CD4 Mem2-like (CD4 TCF1^{+} CD69^{+}) cells, various CD8 subsets, and B cells (Figure S10L), suggestive of coordinated immune niches linked to therapeutic efficacy. In the tumor center, responders showed greater infiltration of most T cell subsets except Tregs, exhausted populations, and the TCF1^{+} CD69^{-} CD4 subset resembling Mem1 (Figure S10L), previously linked to non-response. This region was more myeloid dominated, with accumulation of CD11c^{+} macrophages and CD11b^{+} myeloid cells (Figure S10K), the latter being associated with non-responders (Figure S10L). In contrast, high densities of DCs correlated with response (Figure S10L), underscoring their essential role in sustaining effective local anti-tumor immunity [44–47].

Cell-cell proximity analysis revealed a high density of homotypic CD4 and myeloid clustering (Figure 6B). In responders, the tumor center showed elevated counts of CD4 T cells near CD8 T cells or myeloid cells (Figure 6B), potentially reflecting localized antigen presentation and T cell activation. Analysis of the 10 closest neighbors revealed that CD4 T cells frequently neighbored DCs in both regions and were also close to CD11c^{+} macrophages in the tumor center (Figure 6C). In responders, these neighborhoods were additionally enriched with progenitor-like CD8 T cells (TCF1^{+} GzmK$^{+/-}$) (Figure 6C and 6E). Using a proximity score to evaluate how frequently two cell types interact relative to their population size, TCF1^{+} CD8 T cells and DCs were more frequently associated with CD4 T cells in responders (Figure 6D and 6E, Figure S11A), suggesting coordinated spatial interactions supporting anti-tumor responses. CD8 T cells were also frequently surrounded by DCs, and at the invasive margin, responder CD8 neighborhoods were enriched with early CD4 Mem2-

like cells (CD4 TCF1$^+$ CD69$^+$) (Figure S11B-S11D). In contrast, in non-responders, CD4 T cell neighborhoods at the invasive margin showed increased proximity with CD11b$^+$ myeloid cells (Figure 6C), suggestive of less stimulator, more suppressive niches.

To further investigate the organization of these interactions, we analyzed higher-order structures defined by triads of CD4 T cells, stem-like CD8 TCF1$^+$ GzmK$^+$/$^-$ cells, and APCs (B cells, DCs, macrophages, or CD11b$^+$ myeloid cells HLA-DR$^+$) in close proximity. These triadic arrangements were more frequent in responders (Figure 6F), with DCs and B cells dominating at the invasive margin, and CD11c$^+$ macrophages and DCs predominating in the tumor center (Figure 6G and 6H; Figure S11E). Overall, the enrichment of structured niches containing CD4 T cells, progenitor-like CD8 T cells and specialized APCs in responders underscores a coordinated immune architecture that supports sustained CD8 T cell responses and effective therapy in MSS CRLM.

Discussion

Although neoadjuvant chemotherapy is the standard of care for MSS CRLM, only a minority of patients achieve meaningful tumor regression, and long-term outcomes remain poor. The limited efficacy of immunotherapies such as PD-1 blockades further emphasizes that therapeutic response requires more than reinvigoration of CD8 T cells. In this study, we identify spatially organized T cell populations associated with neoadjuvant treatment response, notably Th1-like memory CD4 (CD4 Mem2) and stem-like CD8 T cells positioned alongside APCs. These findings uncover key features of effective anti-tumor immunity in CRLM and offer a foundation for improved prognostic and therapeutic strategies.

High-throughput profiling revealed spatially distinct immune niches in CRLM. Immune cells accumulated at the invasive margin, while the tumor core was devoid of cytotoxic and innate lymphocytes and rather featured Tregs and terminally exhausted CD8 T cells, consistent with previous reports [29,43]. Despite this suppressive milieu, CD4 memory T cells were the predominant lymphocyte population across regions, and their general transcriptional features appeared preserved following therapy. Their persistence aligns with prior observations that CD4 T cells are less chemotherapy-sensitive than CD8 T cells [42]. Given their central role in coordinating immune responses and licensing APCs [22,23,49,50], this resilience and spatial enrichment suggest a critical function in modulating therapeutic response in CRLM. In responders, a subset of CD4 Mem2 cells (CD45RO$^+$ CD127$^+$ CD69$^+$ CD161$^-$) expressing CD40L, TNF and IFN-γ, likely supports APCs via CD40 signaling and, thereby enhancing CD8 T cell infiltration and function [51–54]. This is particularly relevant in MSS CRLM, where APC dysfunction is well documented [24–26]. Although CD40 agonists can reverse myeloid suppression [55–57], promote Th1 polarization [58] and remodel the TME [59,60], their single-agent efficacy may be constrained by the low neoantigen load in MSS CRC, underscoring the need for CD4 help in the tumor niche and the potential of combination strategies with chemotherapy or vaccines to overcome resistance [24,61–64].

In responders to neoadjuvant therapy, Th1-like CD4 Mem2 co-localized with CD8 memory subsets, revealing coordinated cellular networks that sustain anti-tumor immunity. These CD8 populations included stem-like memory cells (CD8 Mem) with limited clonal expansion, consistent with a self-renewing, exhaustion-resistant pool [47,65,66], as well as GzmK$^+$ transitional effector cells (CD8 EM) [29,66–69], previously linked to favorable outcomes in CRC [43,70]. The spatial proximity of these CD8 and CD4 T cells to APCs suggests the existence of specialized niches essential for maintaining effector function under low antigenic pressure. TCF1$^+$ progenitor-like CD8 T cells rely on APC-derived co-stimulation for differentiation [71], highlighting the functional relevance of CD4-centered interactions. While intratumoral APCs are increasingly recognized for sustaining progenitor T cells [44–47], our data reveal a previously underappreciated role for CD4 T cells in instructing these niches. In responders, triads of CD4 T cells, stem-like or GzmK$^+$ CD8 T cells, and DCs were observed in both tumors centers and invasive margins, with B cells occasionally present at the margins, potentially contributing to anti-tumor IgG responses [72] or APC activity. CD11c$^+$ macrophages in tumor centers similarly engaged in triad-like interactions, suggesting additional antigen-presenting functions. Together, these CD4 orchestrated niches likely serve as hubs for sustained T cell activation and fate decisions, mirroring observations in murine melanoma models and hepatocellular carcinoma where CD4-APC interactions reprogram intratumoral CD8 T cells to enhance anti-tumor immunity [73,74].

Non-responders were enriched for Tregs and less activated, stem-like CD4 memory T cells (CD4 Mem1, CD127$^+$ CD69$^-$) exhibiting NF-κB activation, oxidative stress, hypoxia and TGF-β signaling, consistent with an immunosuppressive microenvironment. This aligns with prior reports of SPP1$^+$ macrophages hypoxic niches of non-responders, which promote TGF-β signaling and Treg induction [29,30,75]. TGF-β and Tregs suppress Th1 differentiation [76], likely contributing to the reduced Th1-like memory CD4 T observed [77,78]. Prior work shows that stem-like tumor-specific CD4 T cells regain Th1 polarization and enhance CD8 T cell responses upon Treg depletion [77]. Chemotherapy may further shift myeloid cells toward a less activated state [42], underscoring the importance of CD4-mediated co-stimulation, particularly via CD40, for APC reprogramming and effective anti-tumor immunity. Consistently, CD4 T cell enrichment and activation of IFN-γ and TNF pathways correlate with chemotherapy responsiveness in breast cancer [79].

Our findings place Th1-like memory CD4 T cells at the center of spatially organized immune niches in MSS CRLM, where they interact with progenitor-like CD8 T cells and specialized APCs to sustain anti-tumor immunity. These niches are enriched in responders to neoadjuvant therapy and associate with favorable prognosis, underscoring the pivotal role of CD4-driven immunity in shaping therapeutic outcomes. By resolving the cellular architecture and signaling networks that underly neoadjuvant treatment response, this work provides a rationale for combinatorial approaches, such as enhancing myeloid licensing and Th1 polarization with CD40 agonists, to reinforce

CD4-APC-CD8 crosstalk and overcome immune resistance in MSS CRLM and other immunologically cold tumors.

Resource availability

Lead contact

Further information and requests for resources and reagents should be directed to Sònia Tugues (tugues@immunology.uzh.ch) and Bettina Sobottka (AnnaBettina.Sobottka-Brillout@usz.ch)

Material availability

This study did not generate new reagents.

Data and code availability

The code used for all analysis and data are available upon demand.

Acknowledgements

We are grateful to Susanne Dettwiler and Fabiola Prutek from the Department of Pathology and Molecular Pathology (University Hospital Zurich) for their contributions to sample handling, tissue microarray production and subsequent processing. We also thank the Functional Genomics Center Zurich (University of Zurich) and the Cytometry Facility (University of Zurich) for their technical support. Specifically, we thank Qin Zhang for processing the libraries for the Rhapsody workflow and Falko Noé for pre-processing the sequencing data and sharing his expertise on computational analyses. We acknowledge Vadir Lopez-Salmeron and Eva Sofía Sánchez Quant from BD Bioscience for their valuable input in setting up the Rhapsody workflow. Additionally, we thank Victor Kreiner, Can Ulutekin Alvarez (Institute of Experimental Immunology, University of Zurich) and Florian Ingelfinger (University of Freiburg) for sharing their expertise on computational analyses.

This work was supported by grants from the Swiss National Science Foundation (PR00P3_179775) to S.T. and (320030-228252) to S.T and B.S, the Swiss Cancer Research Foundation (KFS-5420-02-2021) to S.T., the Candoc from UZH to M.M. (21-026), the Sassella Foundation to C.S. and S.T., the Vontobel Foundation to S.T., the Novartis Foundation to S.T., the Olga Mayenfisch Foundation to S.T. and the Wilhelm Sander Foundation to S.T.

Author contributions

M.M designed, conducted, analysed the experiments and wrote the first draft of the manuscript. G.L., M.V., E.F., and F.W. supported patient sample collection and the generation of the patient bank. N.N., M.V., F.W., G.L., E.F., S.K., J.S., S.B., and C.S. assisted with flow cytometry experiments. P.J.A., E.G.V., A.K. and S.D. conducted immunofluorescence staining and imaging of slides, with P.J.A. and F.W. supporting

the data analysis. T.W. assisted with the Rhapsody experiment. C.S and G.L. performed all cell sorting. V.K.V. and B.S. provided expert pathological evaluations. N.N., X.F., F.M., F.W., B.B., A.M., provided intellectual input and conceptual advice. S.T. and B.S. designed, co-supervised the study and co-wrote the manuscript with M.M., with input of all coauthors.

Declaration of interests

The authors declare no competing interests.

Declaration of generative AI and AI-assisted technologies

During the preparation of this work, the author(s) used ChatGPT (4.1, OpenAI) to improve the language of the initial manuscript draft. The authors subsequently reviewed and extensively edited the content and take full responsibility for the published article. The same Ai-assisted technologies was also used to generate plotting code for some figures, which was thoroughly verified by authors.

Supplemental information

Document S1. Figure S1-S11, Tables S1-S5 and S9.
Table S6. Differentially expressed genes in CD4 T cells from Rhapsody analysis
Table S7. Differentially expressed genes in CD8 T cells from Rhapsody analysis
Table S8. Rhapsody signature gene list

Figure title and legend

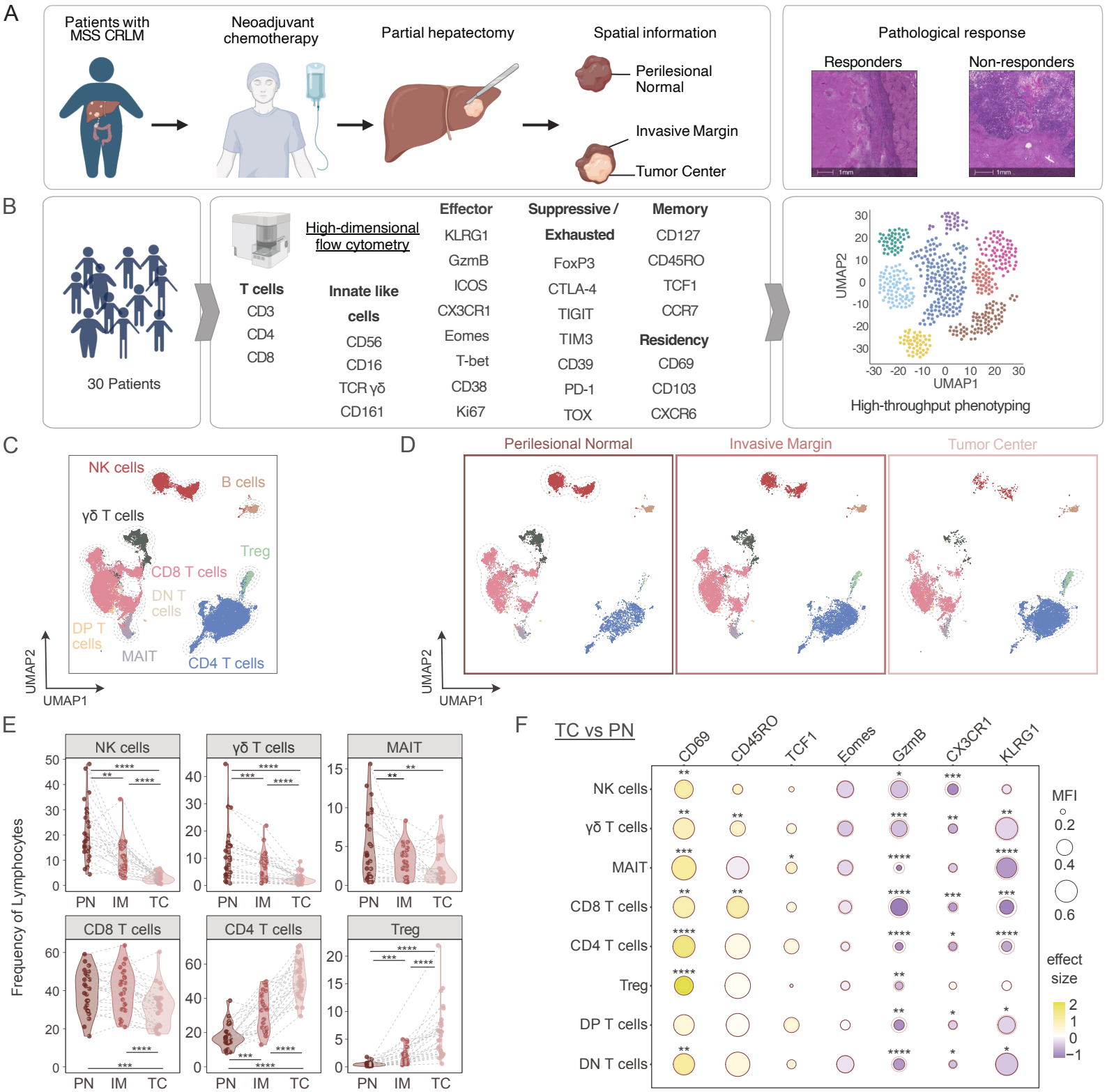
A
Patients with MSS CRLM
Neoadjuvant chemotherapy
Partial hepatectomy
Spatial information
Perilesional Normal
Invasive Margin
Tumor Center
Pathological response
Responders
Non-responders
B
30 Patients
High-dimensional flow cytometry
T cells
CD3
CD4
CD8
Innate like cells
CD56
CD16
TCR γδ
CD161
Effector
KLRG1
GzmB
ICOS
CX3CR1
Eomes
T-bet
CD38
Ki67
Suppressive / Exhausted
FoxP3
CTLA-4
TIGIT
TIM3
CD39
PD-1
TOX
Memory
CD127
CD45RO
TCF1
CCR7
Residency
CD69
CD103
CXCR6
UMAP2
UMAP1
High-throughput phenotyping
C
NK cells
B cells
γδ T cells
Treg
CD8 T cells
DN T cells
DP T cells
MAIT
CD4 T cells
UMAP2
UMAP1
D
Perilesional Normal
Invasive Margin
Tumor Center
UMAP2
UMAP1
E
NK cells
γδ T cells
MAIT
CD8 T cells
CD4 T cells
Treg
Frequency of Lymphocytes
PN
IM
TC
F
TC vs PN
CD69
CD45RO
TCF1
Eomes
GzmB
CX3CR1
KLRG1
NK cells
γδ T cells
MAIT
CD8 T cells
CD4 T cells
Treg
DP T cells
DN T cells
MFI
0.2
0.4
0.6
effect size
2
1
0
−1

Figure 1. CD4 T cell dominance and cytotoxic cell exclusion characterize the CRLM tumor microenvironment. (A) Graphical summary of the patient history prior to sample collection, the dissection into three spatially distinct regions, and the clinically assessed pathological response. (B) Experimental workflow for high-dimensional flow cytometry analysis. (C) UMAP displaying 76,000 cells (1,000 cell per sample), colored by cluster. (D) UMAP displaying 10,000 cells per region (from 27 tumor center, 25 invasive margin and 24 perilesional normal), colored by cluster. (E) Violin plots showing the frequency of the major lymphoid populations across regions. (F) Bubble plot showing the median normalized fluorescence intensity of selected markers, comparing marker expression in the tumor center (TC; black circle) and perilesional normal (PN; light red circle) tissue. The bubble plot is colored by effect size (Cohen's D), indicating upregulation (yellow) or downregulation (blue) of marker expression in the TC compared to PN tissue. (E,F) Statistical significance was determined using paired Wilcoxon tests, corrected for multiple comparisons using the Benjamini-Hochberg method. Significance levels are displayed as follows, * pvalue adjusted <0.05, ** pvalue adjusted <0.01, *** pvalue adjusted < 0.001,**** pvalue adjusted <0.0001.

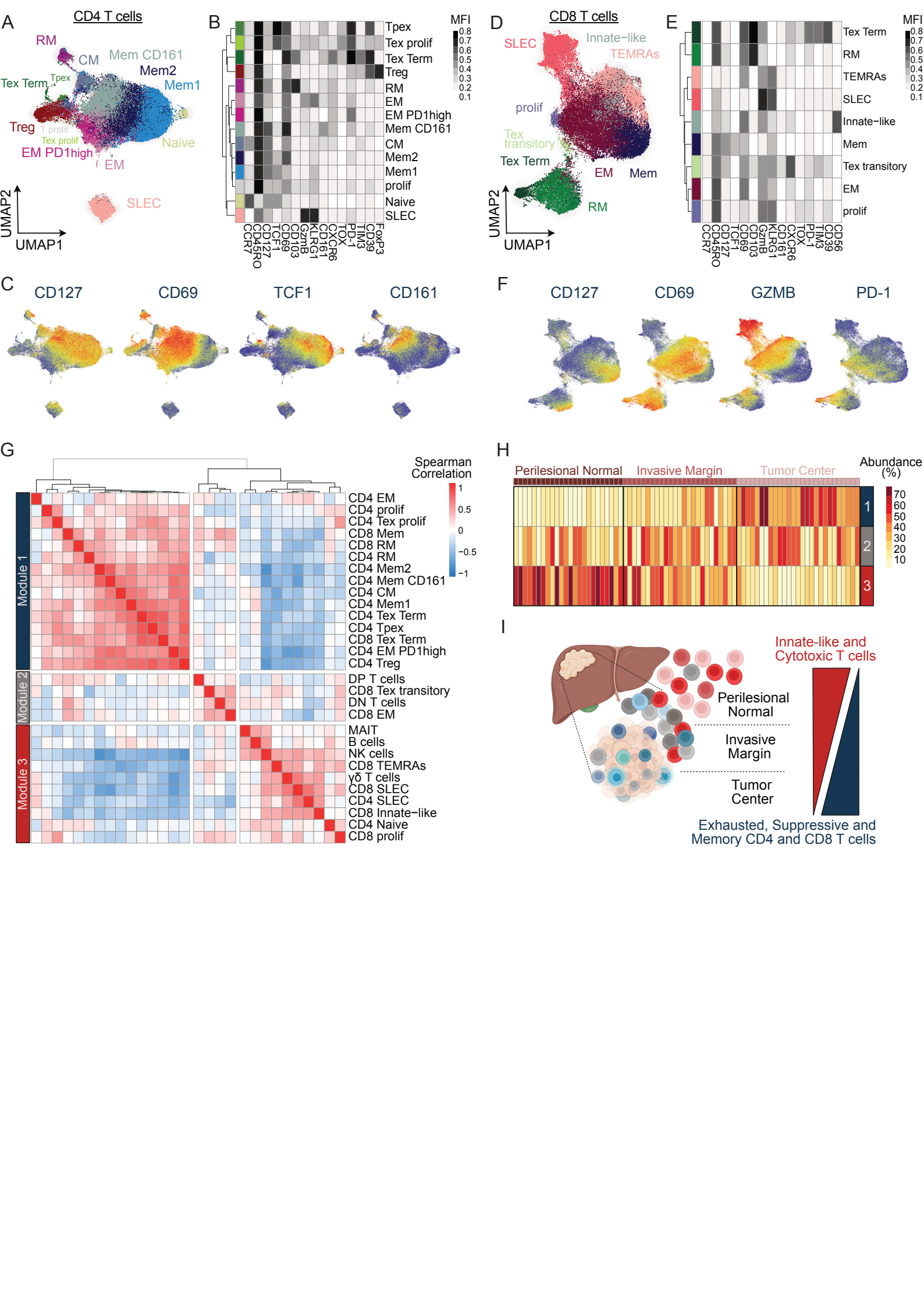
A
CD4 T cells
RM
CM
Mem CD161
Mem2
Tex Term
Tpex
Mem1
Treg
T prolif
Tex prolif
Naive
EM PD1high
EM
SLEC
UMAP2
UMAP1
B
MFI
0.8
0.7
0.6
0.5
0.4
0.3
0.2
0.1
Tpex
Tex prolif
Tex Term
Treg
RM
EM
EM PD1high
Mem CD161
CM
Mem2
Mem1
prolif
Naive
SLEC
CCR7
CD45RO
CD127
TCF1
CD69
CD103
GzmB
KLRG1
CD161
CXCR6
TOX
PD-1
TIM3
CD39
FoxP3
D
CD8 T cells
SLEC
Innate−like
TEMRAs
prolif
Tex transitory
Tex Term
EM
Mem
RM
UMAP2
UMAP1
E
MFI
0.8
0.7
0.6
0.5
0.4
0.3
0.2
0.1
Tex Term
RM
TEMRAs
SLEC
Innate−like
Mem
Tex transitory
EM
prolif
CCR7
CD45RO
CD127
TCF1
CD69
CD103
GzmB
KLRG1
CD161
CXCR6
TOX
PD-1
TIM3
CD39
CD56
C
CD127
CD69
TCF1
CD161
F
CD127
CD69
GZMB
PD-1
G
Spearman Correlation
1
0.5
0
−0.5
−1
Module 1
Module 2
Module 3
CD4 EM
CD4 prolif
CD4 Tex prolif
CD8 Mem
CD8 RM
CD4 RM
CD4 Mem2
CD4 Mem CD161
CD4 CM
CD4 Mem1
CD4 Tex Term
CD4 Tpex
CD8 Tex Term
CD4 EM PD1high
CD4 Treg
DP T cells
CD8 Tex transitory
DN T cells
CD8 EM
MAIT
B cells
NK cells
CD8 TEMRAs
γδ T cells
CD8 SLEC
CD4 SLEC
CD8 Innate−like
CD4 Naive
CD8 prolif
H
Perilesional Normal
Invasive Margin
Tumor Center
Abundance (%)
70
60
50
40
30
20
10
1
2
3
I
Innate-like and Cytotoxic T cells
Perilesional Normal
Invasive Margin
Tumor Center
Exhausted, Suppressive and Memory CD4 and CD8 T cells

Figure 2. The tumor center is enriched in memory, exhausted, and suppressive T cells. (A) UMAP of CD4 T cells created with 1,000 cells per sample when possible and displaying 60,000 cells (20,000 cells per region), colored by cluster. (B) Heatmap showing the mean of the normalized expression of selected markers for each CD4 T cell cluster. (C) UMAP of CD4 T cells displaying 74,899 cells (1,000 cells per sample when possible), colored by normalized MFI value. (D) UMAP of CD8 T cells created with 1,000 cells per sample when possible and displaying 60,000 cells (20,000 cells per region), colored by cluster. (E) Heatmap showing the mean normalized expression of selected markers for each CD8 T cell cluster. (F) UMAP of CD8 T cells displaying 74,124 cells (1,000 cells per sample when possible) and colored by normalized MFI value. (G) Spearman correlation between lymphoid subsets frequencies with hierarchical clustering identifying three cellular modules. Analysis includes 76 samples from the perilesional normal, invasive margin and tumor center regions, all similarly processed. (H) Percentage abundance of the three modules across regions, with each column representing a patient sample separated by regions. Module scores were calculated as the average of the normalized frequency (0 to 1) of all immune subsets within each module, and expressed as percentages so that the total per patient equals 100%. See Methods for details. (I) Graphical representation of the lymphoid subsets differentially represented in the three spatially distinct regions (perilerional normal, invasive margin and tumor center).

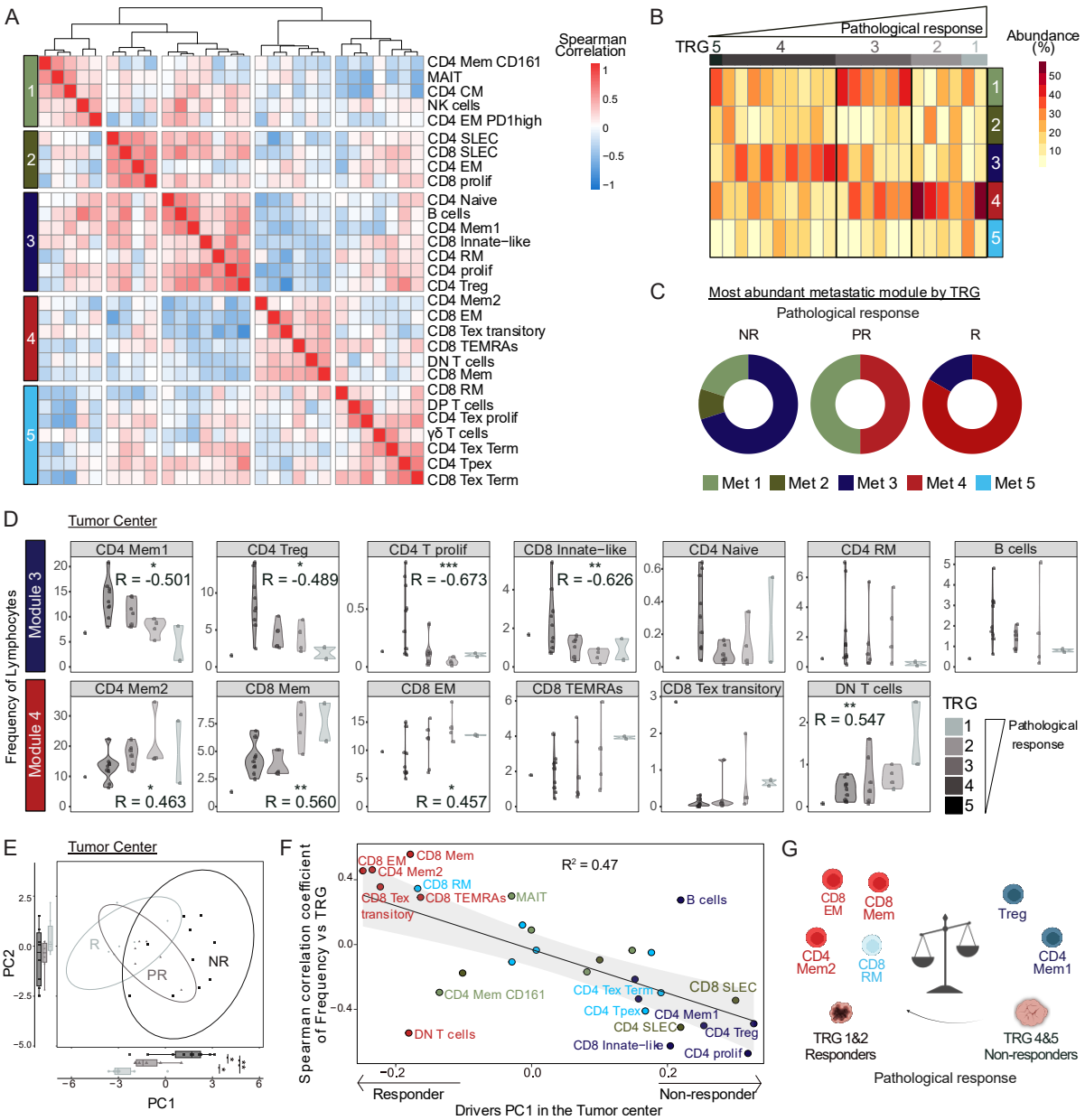
A
Spearman Correlation
CD4 Mem CD161
MAIT
CD4 CM
NK cells
CD4 EM PD1high
CD4 SLEC
CD8 SLEC
CD4 EM
CD8 prolif
CD4 Naive
B cells
CD4 Mem1
CD8 Innate−like
CD4 RM
CD4 prolif
CD4 Treg
CD4 Mem2
CD8 EM
CD8 Tex transitory
CD8 TEMRAs
DN T cells
CD8 Mem
CD8 RM
DP T cells
CD4 Tex prolif
γδ T cells
CD4 Tex Term
CD4 Tpex
CD8 Tex Term
B
Pathological response
TRG 5 4 3 2 1
Abundance (%)
C
Most abundant metastatic module by TRG
Pathological response
NR
PR
R
Met 1
Met 2
Met 3
Met 4
Met 5
D
Tumor Center
Frequency of Lymphocytes
Module 3
Module 4
CD4 Mem1
R = -0.501
CD4 Treg
R = -0.489
CD4 T prolif
R = -0.673
CD8 Innate−like
R = -0.626
CD4 Naive
CD4 RM
B cells
CD4 Mem2
R = 0.463
CD8 Mem
R = 0.560
CD8 EM
R = 0.457
CD8 TEMRAs
CD8 Tex transitory
DN T cells
R = 0.547
TRG
Pathological response
E
Tumor Center
PC2
PC1
R
PR
NR
F
Spearman correlation coefficient of Frequency vs TRG
R² = 0.47
CD8 EM
CD8 Mem
CD4 Mem2
CD8 RM
CD8 Tex transitory
CD8 TEMRAs
MAIT
B cells
CD4 Mem CD161
CD4 Tex Term
CD8 SLEC
CD4 Tpex
CD4 Mem1
CD4 SLEC
CD4 Treg
DN T cells
CD8 Innate−like
CD4 prolif
Responder
Non-responder
Drivers PC1 in the Tumor center
G
CD8 EM
CD8 Mem
Treg
CD4 Mem2
CD8 RM
CD4 Mem1
TRG 1&2 Responders
TRG 4&5 Non-responders
Pathological response

Figure 3. Distinct CD4 and CD8 T cell modules correlate with neoadjuvant treatment response. (A) Spearman correlation between lymphoid subsets frequencies, followed by hierarchical clustering on the spearman correlation coefficients, identifying five metastatic modules in the tumor center. (B) Percentage abundance of the five metastatic modules across TRG score, with each column representing a patient sample and its associated TRG. Module scores were calculated as the average of the normalized frequency of all immune subsets within each module, and expressed as percentages so that the total per patient equals 100%. See Methods for details. (C) Distribution of the most abundant module per patient across all pathological response groups: responders (R, TRG 1&2) includes two patients with TRG1 and four with TRG2; partial responders (PR, TRG3) include seven patients; non-responders (NR, TRG 4&5) includes nine patients with TRG 4 and one with TRG 5. (D) Correlation between lymphocyte frequencies and TRG score for all cell types in Metastatic Modules 3 and 4. Statistical significance was determined using rank-based Spearman monotonicity, displaying the correlation coefficient (R) of lymphocyte frequency and TRG score and significance levels as followed, * pvalue <0.05, ** pvalue <0.01, *** pvalue < 0.001. Positive correlation coefficient (R) indicates association with low TRG (i.e. responders). (E) PCA based on the frequency of all clusters from the tumor center, per patient, grouped by pathological response: responders (R, TRG 1 & 2, circles), partial responders (PR, TRG 3, triangles), and non-responders (NR, TRG 4 & 5, squares). Boxplots along the axes display the distribution of PC1 and PC2 values per patient grouped by response group. Statistical significance was determined using paired Wilcoxon tests, corrected for multiple comparisons using the Benjamini-Hochberg method. Significance levels are displayed as follows, * pvalue adjusted <0.05, ** pvalue adjusted <0.01, *** pvalue adjusted < 0.001,**** pvalue adjusted <0.0001. (F) Correlation between the Spearman correlation coefficient (R) of lymphocyte frequency and TRG score (y axis) and the PC1 distance of the immune subsets (x axis). Linear regression shows a positive correlation with R^2=0.47. (G) Graphical representation of the lymphoid landscape dynamics across pathological responders and non-responders to neoadjuvant treatment. Analyses were performed on the tumor center region of 22 patients from which the TRG information was available.

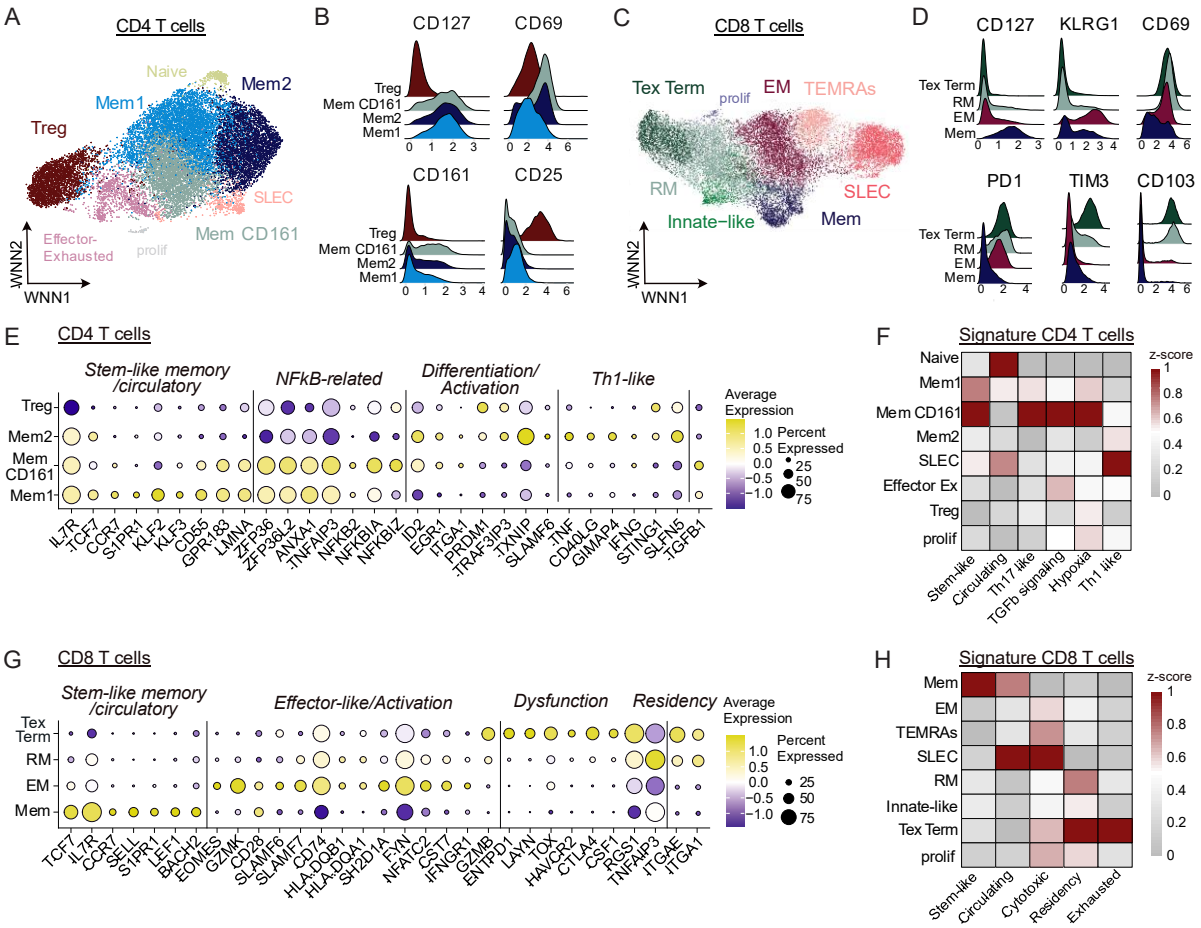
A
CD4 T cells
Naive
Mem2
Mem1
Treg
SLEC
Mem CD161
Effector-
Exhausted
prolif
WNN2
WNN1
B
CD127
CD69
CD161
CD25
Treg
Mem CD161
Mem2
Mem1
C
CD8 T cells
Tex Term
prolif
EM
TEMRAs
RM
SLEC
Innate−like
Mem
D
CD127
KLRG1
CD69
PD1
TIM3
CD103
Tex Term
RM
EM
Mem
E
CD4 T cells
Stem-like memory /circulatory
NFkB-related
Differentiation/ Activation
Th1-like
Average Expression
Percent Expressed
F
Signature CD4 T cells
z-score
Naive
Mem1
Mem CD161
Mem2
SLEC
Effector Ex
Treg
prolif
Stem-like
Circulating
Th17 like
TGFb signaling
Hypoxia
Th1 like
G
CD8 T cells
Stem-like memory /circulatory
Effector-like/Activation
Dysfunction
Residency
Average Expression
Percent Expressed
H
Signature CD8 T cells
z-score
Mem
EM
TEMRAs
SLEC
RM
Innate-like
Tex Term
prolif
Stem-like
Circulating
Cytotoxic
Residency
Exhausted

575 **Figure 4. Responder-associated T cells display Th1-like CD4 and CD8 progenitor signatures.** (A) Weighted Nearest Neighbor Analysis (WNN) on CD4 T cells from CRLM patients, using integrated transcriptomic and proteomic data for clustering, combining all regions from eight patients (15,470 cells). (B) Histogram showing the z-score of centered log ratio-normalized antibody-derived tag expression of CD127, CD69, CD161 and CD25 protein expression on selected CD4 T cell subsets. (C)
580 WNN of CD8 T cells from CRLM patients, using integrated transcriptomic and proteomic data for clustering and combining all regions from eight patients (19,767 cells). (D) Histogram showing the z-score of centered log ratio-normalized antibody-derived tag expression of CD127, KLRG1, PD-1 and CD28 protein expression on selected CD8 T cell subsets. (E) Dotplot showing the expression levels of selected genes from the top differentially express gene analysis (genes with positive log fold change, a
585 minimum detection rate of 25%, and a log fold change threshold of 0.25). (F) Heatmap showing the z-score of defined signatures across CD4 T cell clusters. (G) Dotplot showing the level of expression of selected genes from the top differentially express gene analysis (genes with positive log fold change, a minimum detection rate of 25%, and a log fold change threshold of 0.25). (H) Heatmap showing the z-score of defined signatures across CD8 T cell clusters.

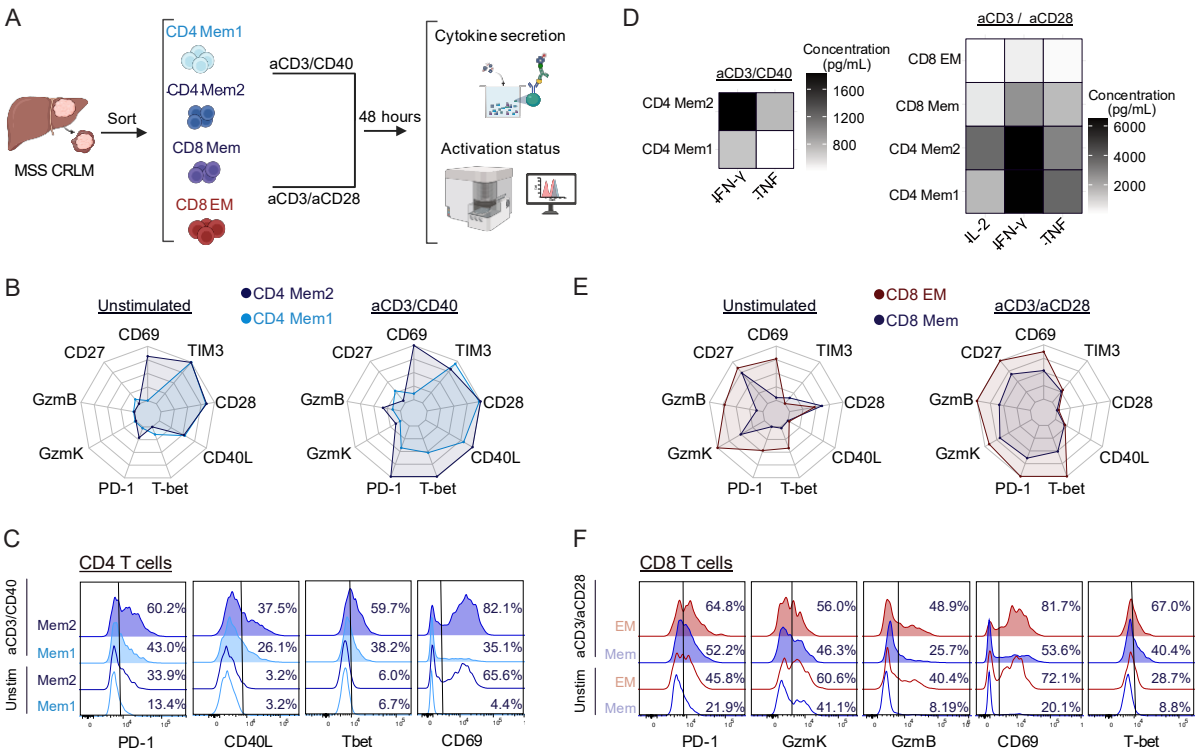
A
MSS CRLM
Sort
CD4 Mem1
CD4 Mem2
CD8 Mem
CD8 EM
aCD3/CD40
aCD3/aCD28
48 hours
Cytokine secretion
Activation status
D
aCD3/CD40
Concentration (pg/mL)
1600
1200
800
CD4 Mem2
CD4 Mem1
IFN-γ
TNF
aCD3 / aCD28
CD8 EM
CD8 Mem
CD4 Mem2
CD4 Mem1
Concentration (pg/mL)
6000
4000
2000
IL-2
IFN-γ
TNF
B
Unstimulated
CD4 Mem2
CD4 Mem1
aCD3/CD40
CD69
TIM3
CD28
CD40L
T-bet
PD-1
GzmK
GzmB
CD27
E
Unstimulated
CD8 EM
CD8 Mem
aCD3/aCD28
C
CD4 T cells
aCD3/CD40
Unstim
Mem2
Mem1
60.2%
43.0%
33.9%
13.4%
37.5%
26.1%
3.2%
3.2%
59.7%
38.2%
6.0%
6.7%
82.1%
35.1%
65.6%
4.4%
PD-1
CD40L
Tbet
CD69
F
CD8 T cells
aCD3/aCD28
Unstim
EM
Mem
64.8%
52.2%
45.8%
21.9%
56.0%
46.3%
60.6%
41.1%
48.9%
25.7%
40.4%
8.19%
81.7%
53.6%
72.1%
20.1%
67.0%
40.4%
28.7%
8.8%
PD-1
GzmK
GzmB
CD69
T-bet

590

Figure 5. CD4 Mem2 T cells show enhanced Th1 activity, while CD8 memory subsets display complementary functions. (A) Experimental design: CD4 Mem1 (CD45RO$^+$ CD127$^+$ CD69$^-$), CD4 Mem2 (CD45RO$^+$ CD127$^+$ CD69$^+$ CD161$^-$), CD8 Mem (CD45RO$^+$ CD127$^+$ CD69$^-$) and CD8 EM (CD45RO$^+$ CD127$^-$ CD69$^+$) were sorted (according to the sorting strategy Figure S8B) and stimulated for 48 hours with suboptimal concentrations of CD3 agonist (0.5µg/mL) combined with either CD40 recombinant protein (1µg/mL; aCD3/CD40) or a CD28 agonist (1µg/mL; aCD3/aCD28). Activation status and cytokine production in the medium were assessed using flow cytometry-based measurements. (B) Radar plots showing the protein expression of nine functional markers comparing CD4 Mem1 and CD4 Mem2, unstimulated (left panel) or stimulated with aCD3/CD40 (right panel). The axis limits for the radar plots are based on the minimum and maximum median values for each marker, determined across all groups (CD4 Mem1, CD4 Mem2, CD8 Mem, and CD8 EM) and under all stimulation conditions (unstimulated, aCD3/CD40, and aCD3/aCD28). (C) Histograms showing the fluorescence intensity for PD-1, CD40L, T-bet and CD69 on CD4 Mem1 and CD4 Mem2, unstimulated or stimulated with aCD3/CD40. (D) Heatmaps showing the estimated concentration of IFN-γ, TNF and IL-2 in the supernatant of CD4 Mem1, CD4 Mem2, CD8 Mem and CD8 EM following aCD3/CD40 (left panel) or aCD3/aCD28 (right panel) stimulation. (E) Radar plots comparing the protein expression of nine functional markers between CD8 memory and CD8 EM, unstimulated (left panel) or stimulated with aCD3/aCD28 (right panel). (F) Histograms showing the fluorescence intensity for PD-1, GzmK, GzmB, CD69 and T-bet on CD8 Mem and CD8 EM, unstimulated or stimulated with aCD3/aCD28

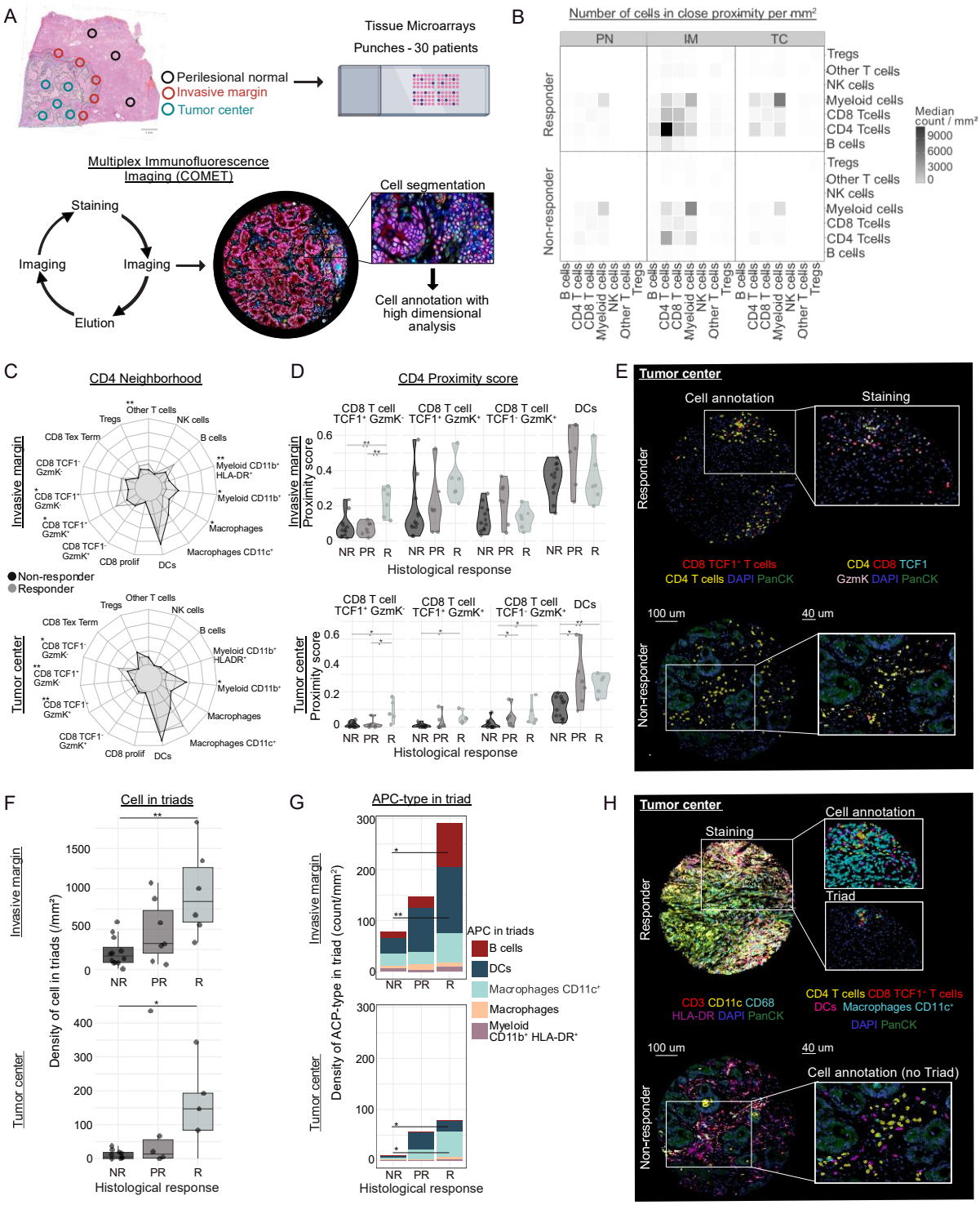
A
Perilesional normal
Invasive margin
Tumor center
Tissue Microarrays
Punches - 30 patients
Multiplex Immunofluorescence Imaging (COMET)
Staining
Imaging
Imaging
Elution
Cell segmentation
Cell annotation with high dimensional analysis
B
Number of cells in close proximity per mm²
PN
IM
TC
Responder
Non-responder
Tregs
Other T cells
NK cells
Myeloid cells
CD8 Tcells
CD4 Tcells
B cells
Median count / mm²
9000
6000
3000
0
C
CD4 Neighborhood
Invasive margin
Tumor center
Non-responder
Responder
Other T cells
NK cells
B cells
Myeloid CD11b⁺ HLA-DR⁺
Myeloid CD11b⁺
Macrophages
Macrophages CD11c⁺
DCs
CD8 prolif
CD8 TCF1⁺ GzmK⁺
CD8 TCF1⁺ GzmK⁻
CD8 TCF1⁻ GzmK⁺
CD8 TCF1⁻ GzmK⁻
CD8 Tex Term
Tregs
D
CD4 Proximity score
CD8 T cell TCF1⁺ GzmK⁻
CD8 T cell TCF1⁺ GzmK⁺
CD8 T cell TCF1⁻ GzmK⁺
DCs
Invasive margin Proximity score
Tumor center Proximity score
NR PR R
Histological response
E
Tumor center
Cell annotation
Staining
Responder
Non-responder
CD8 TCF1⁺ T cells
CD4 T cells DAPI PanCK
CD4 CD8 TCF1
GzmK DAPI PanCK
100 um
40 um
F
Cell in triads
Invasive margin
Tumor center
Density of cell in triads (/mm²)
NR PR R
Histological response
G
APC-type in triad
Invasive margin
Tumor center
Density of ACP-type in triad (count/mm²)
APC in triads
B cells
DCs
Macrophages CD11c⁺
Macrophages
Myeloid CD11b⁺ HLA-DR⁺
NR PR R
Histological response
H
Tumor center
Staining
Cell annotation
Triad
Responder
Non-responder
CD3 CD11c CD68
HLA-DR DAPI PanCK
CD4 T cells CD8 TCF1⁺ T cells
DCs Macrophages CD11c⁺
DAPI PanCK
100 um
40 um
Cell annotation (no Triad)

Figure 6. Spatial coordination of CD4 memory, CD8 T cells and APCs defines treatment-responsive niches. (A) Punches of 600 µm diameter guided by H&E staining were assembled from the tumor center, the invasive margin and the perilesional normal tissue of our cohort of 30 MSS CRLM patients (Figure S1A), and analyzed using Lunaphore COMET multiplex imaging technology. (B) Heatmap showing the median density of interaction, i.e. counts of cell-cell proximities within a 15 radius normalized by the segmented tissue area in mm² per patient and averaged by region and response group. (C) Radar plots showing the mean cell type composition of CD4 neigbhorhood in the invasive margin and tumor center per response group. For each CD4 T cells, the 10 closest non-CD4 neighboring cells were retrieved and the proportion of each neighbor cell type per patient was then calculated. The radial axis of the radar plot is scaled to a maximum of 35%. Statistical comparisons between response groups were performed using permutation-based independence tests, with p-values adjusted using the Benjamini–Hochberg method. Significance levels are indicated as: * pvalue adjusted <0.05, ** pvalue adjusted <0.01. (D) Violin plots showing the proximity score to CD4 T cells per-patient: ratio of the number of cells of identified interactions by the total number of cells of the interacting type. Statistical comparisons were performed separately for each neighbor type and region, using an initial Kruskal–Wallis test, followed by Benjamini–Hochberg-adjusted pairwise Wilcoxon rank-sum tests for all group pairs (responder, mid, non-responder). Significance is depicted as follows: * pvalue adjusted <0.05 and ** pvalue adjusted <0.01. (E) Representative images from the TMA at the tumor center of a responder (TRG 2) and non-responder (TRG 4) patient sample. Left panel shows CD4 T cells and CD8 TCF1^{+} GzmK$^{+/-}$ T annotated cells. Right panel: Zoom in showing the staining of selected markers used for phenotyping. (F) Box plots showing the density (i.e. count / mm²) of cells participating in at least one qualifying triad (CD4 T cell, CD8 TCF1^{+} GzmK$^{+/-}$ and APC) across patients, grouped by response and region. (G) Bar plots showing the density of APC-type in triad using the mean across patients per response group and region (D, F, G). Statistical comparisons were performed using unpaired Wilcoxon tests, and depicted as follows: * pvalue <0.05, ** pvalue <0.01, *** pvalue < 0.001 . We used the following abbreviation: NR for non-responders, PR for partial responders, and R for responders. (H) Representative images from the TMA at the tumor center of a responder (TRG 2) and non-responder (TRG 4) patient sample, Left panel: staining of selected myeloid marker on full TMA, Middle panel: Zoom in showing the cell annotated as CD4 T cells and CD8 TCF1^{+} GzmK$^{+/-}$ T cells, Macrophags CD11c^{+} and DCs. Right panel: Zoom in showing the cell participating in at least one qualifying triad.

645 **STAR Methods**

Key resources table

REAGENT or RESOURCE	SOURCE	IDENTIFIER
Antibodies		
Anti-human CXCR6 BV650 clone 13B 1E5	BD Biosciences	743600
Anti-human CCR7 BV785 clone G043H7	Biolegend	353230
Anti-human CX3CR1 BUV661 clone 2A9-1	BD Biosciences	750690
Anti-human CD45RO BUV615 clone UCHL1	BD Biosciences	751167
Anti-human CD103 Biotin clone Ber-ACT8	Biolegend	350220
Anti-human CD3 BUV805 clone UCHT-1	BD Biosciences	612895
Anti-human CD8 BV570 clone RPA-T8	Biolegend	301038
Anti-human TCRgd PE-Cy5 clone IMMU510	Beckman Coulter	IM2662U
Anti-human CD45 PerCp clone HI-30	Biolegend	304025
Anti-human CD16 BUV496 clone 3G8	BD Biosciences	612944
Anti-human CD161 BUV563 clone HP-3G10	BD Biosciences	749223
Anti-human CD19 Super Bright 436 clone HIB19	Thermo Fisher Scientific	62-0199-42
Anti-human CD56 PE/Dazzle 594 clone 5.1H11	Biolegend	362543
Anti-human CD4 Spark Blue 550 clone SK3	Biolegend	344656
Anti-human CD14 Spark NIR clone 63D3	Biolegend	367150
Anti-human PD-1 BV605 clone EH12.2H7	Biolegend	329924
Anti-human CD38 APC-Fire 810 clone HIT2	Biolegend	303550
Anti-human CD69 BV421 clone FN50	Biolegend	310930
Anti-human ICOS BV750 clone C398.4A	Biolegend	313558
Anti-human TIGIT BUV395 clone 741182	BD Biosciences	747845
Anti-human KLRG1 PE-Fire 810 clone SA231A2	Biolegend	367733
Anti-human TIM3 BB700 clone 344823	BD Biosciences	747957
Anti-human CD39 BUV737 clone TU66	BD Biosciences	564726
Anti-human CD127 BV510 clone A019D5	Biolegend	351332
Anti-human CTLA-4 BB790 clone BNI3	BD Biosciences	624296
Anti-human EOMES APC-eFluor 780 clone WD1928	Thermo Fisher Scientific	47-4877-41
Anti-human T-bet BV711 clone 4B10	Biolegend	644820
Anti-human Ki67 BV480 clone SolA15	Thermo Fisher Scientific	414-5698-82
Anti-human FoxP3 PE-Cy7 clone 236A/E7	Thermo Fisher Scientific	25-4777-42
Anti-human TOX PE clone REA473	Miltenyi Biotec	130-120-716
Anti-human Granzyme B AlexaFluor 700 clone GB11	BD Biosciences	560213
Anti-human TCF-1 AlexaFluor 488 clone C63D9	Cell Signaling	6444S
Streptavidin BB630-P2	BD Biosciences	624294
AbSeq Immune Discovery Panel – 30 markers	BD Biosciences	625970
Anti-human CD38 Ab-O AHS0022 HIT2	BD Biosciences	940057
Anti-human CD49d Ab-O AHS0063 9F10	BD Biosciences	940059
Anti-human CD103 Ab-O AHS0001 BER-ACT8	BD Biosciences	940067
Anti-human CD49a Ab-O AHS0101 SR84	BD Biosciences	940094
Anti-human CX3CR1 Olgo AHS0125 2A9-1	BD Biosciences	940216
Anti-human CD122 Olgo AHS0146 MIK-BETA3	BD Biosciences	940232
Anti-human CD43 Olgo AHS0200 1G10	BD Biosciences	940278

Anti-human CD95 Ab-O AHS0023 DX2	BD Biosciences	940037
Anti-human CD45RO Ab-O AHS0036 UCHL1	BD Biosciences	940022
Anti-human CD69 Ab-O AHS0010 FN50	BD Biosciences	940019
Anti-human TCRgd Ab-O AHS0015 B1	BD Biosciences	940057
Anti-human KLRG1 APC clone SA231A2	Biolegend	367715
Anti-human APC Olgo AHS0295 E30-221	BD Biosciences	460078
Anti-human CD39 Ab-O AHS0006 TU66	BD Biosciences	940073
Anti-human CD45 BV758 clone HI-30	Biolegend	304048
Anti-human CD38 BV650 clone HIT2	BD Biosciences	740574
Anti-human CD14 FITC clone 61D3	Thermo Fisher Scientific	11-0149-41
Anti-human CD8 PE clone SK-1	BD Biosciences	345773
Anti-human CD25 R718 clone BC96	BD Biosciences	567575
Anti-human CD45RO PE-Cy7 clone UCHL1	Biolegend	304230
Anti-human CD161 BV785 clone HP-3G10	Biolegend	339930
Anti-human CD127 BV605 clone A019D5	Biolegend	351333
Anti-human CD103 BV510 clone Ber-ACT8	BD Biosciences	743651
Anti-human CD25 PE clone M-A251	Biolegend	356103
Anti-human CD27 BUV563 clone M-T271	BD Biosciences	741366
Anti-human CD28 BV750 clone CD28.2	BD Biosciences	747329
Anti-human TIM3 VioBright FITC clone F38.2E	Miltenyi	130-104-687
Anti-human HLA-DR BUV395 clone G46-6	BD Biosciences	564040
Anti-human CD40L AF647 clone 24-31	Biolegend	310818
Anti-human Granzyme B AF700 clone GB11	BD Biosciences	560213
Anti-human Granzyme K PE-Cy7 clone GM26E7	Biolegend	370515
Anti-human CD3 rabbit	Lunaphore	MR10010
Anti-human FoxP3 mouse	Lunaphore	MR10040
Anti-human CD4 rabbit	Lunaphore	MR10020
Anti-human HLA-DR mouse	DAKO	M0746
Anti-human CD56 rabbit	Lunaphore	MR10060
Anti-human CD8 mouse	DAKO	M7103
Anti-human CD1c mouse	Novus Biologicals	NBP2-70345
Anti-human CD11c rabbit	Lunaphore	MR10070
Anti-human CD68 mouse	Invitrogen	MA5-13324
Anti-human Clec9a rabbit	Abcam	ab222794
Anti-human CD20 mouse	Lunaphore	L26
Anti-human PD-1 rabbit	Lunaphore	MR10120
Anti-human aSMA mouse	DAKO	M0851
Anti-human STAB2 rabbit	Diagnostic Biosystem	RMAB112
Anti-human Granzyme B rabbit	Abcam	ab208586
Anti-human Pan Cytokeratin mouse	Lunaphore	MR10140
Anti-human CD69 rabbit	Abcam	310902
Anti-human TCF1 rabbit	Cell Signaling	2203
Anti-human Granzyme K rabbit	Abcam	ab282703
Anti-human CD11b rabbit	Cell Signaling	48893
Anti-human Ki67 rabbit	Abcam	ab224639
Biological samples		

Fresh tissue from patients with MSS CRLM tumor metastasis biopsies (flow cytometry, rhapsody, ex vivo stimulation)	This work	NA
2 µm sections of Tissue Micro Arrays built from 30 patients with MSS CRLM tumor metastasis biopsies (multiplex)	This work	NA
Patients with CRLM (RNAseq)	Liu et al., 2022 - *Cancer Cell*	NA
Patients with CRLM (RNAseq)	Wu et al., 2022 - *Cancer Discovery*	NA
Chemicals, peptides, and recombinant proteins		
Recombinant Human CD40-Fc Chimera recombinant protein	Biolegend	#777202
anti-CD28 antibody clone CD28.2	ThermoFisher Scientific	16-0289-85
anti-CD3 antibody clone OKT3	ThermoFisher Scientific	16-0037-85
Critical commercial assays		
Debris Removal Solution	Miltenyi Biotec	130-109-398
BD Rhapsody™ Enhanced Cartridge Reagent Kit	BD Biosciences	664887
BD Rhapsody™ Cartridge Kit	BD Biosciences	633733
BD Rhapsody™ cDNA Kit	BD Biosciences	633773
BD Rhapsody™ WTA Amplification Kit	BD Biosciences	633801
BD Rhapsody™ TCR/BCR Amplification Kit	BD Biosciences	665345
BD® Single-Cell Multiplexing Kit	BD Biosciences	633781
LEGENDplex™ HU Th Cytokine Panel	BioLegend	741028
Software and algorithms	version	
QuPath	0.6.0-rc3	
FlowSOM	2.12.0	
FlowJo software	version 10.9.0	
R version	4.4.1	
fmsb package	version 0.7.6	
stats package	version 4.4.1	
Seurat workflow	5.1.0	
package tidyr	1.3.1	
ggpubr package	0.6.0	
effsize package	0.8.1	
coin package	version 1.4.3	
Other		
COMET™ platform (Lunaphore Technologies)		

Experimental model and subject details

Human specimens

All patients were enrolled at the University Hospital Zurich with pathologically diagnosed colorectal adenocarcinoma stage IV. The study was approved by the Ethics Committee (BASEC 2018-02282), and written informed consent was obtained from all participants fresh tumor and adjacent normal tissue samples from the colorectal liver metastasis surgical resection specimens were obtained by a board-certified pathologist (B.S.). Thirty colorectal cancer patients with liver metastases, including

eleven females and nineteen males aged 51 to 80 years (median: 65), were analyzed using high-dimensional flow cytometry.

660 Patients treated with neoadjuvant chemotherapy received either Oxiplatin/Cabecetabine, Folfiri, Folfoxiri, or Folfox regiments; combined or not with targeted therapy Bevacizumab (anti-VEGF-A), Cetuximab or Panitumumab (anti-EGFR) as indicated per cohort in Figure S1A, Figure S7A and Figure S9A. Response to neoadjuvant therapy was assessed by board-certified pathologists using the TRG 665 according to the Rubbia-Brandt classification system [8] based on the proportion of tumor cell and fibrosis observed in H&E stained CRLM FFPE sample. Patients were categorized as responders (TRG 1&2), partial responders (TRG3) and non-responders (TRG 4&5). The flow cytometry analysis and multiplex imaging were performed on a cohort of 30 patients (Figure S1A). Among the 30 patients analysed, 670 two patients were treatment-naive, and three did not have TRG information. Thus, a total of 25 patients were included in the analysis of the relationship between response to neoadjuvant therapy and the immune landscape based on TRG. The clinical characteristics and sample regions available for each patient are summarized in Figure S1A. Eight colorectal cancer patients with liver metastases (Figure S7A) were 675 included in the sequencing analysis using Rhapsody technology, including four females and four males, aged 36 to 70 years (median: 58). All patients had been treated with NAC, and patients 25 and 28 were also part of the cohort of 30 patients analyzed by high-dimensional flow cytometry. The clinical characteristics and sample regions available for each patient are summarized in Figure S7A. Thirteen colorectal 680 cancer patients with liver metastases (Figure S9A), including four females and nine males, age 41 to 77 years (median: 63), were included in the ex vivo stimulation experiment. The clinical characteristics and the sample regions available for each patient are summarized in Figure S8A.

685 **Method details**

Single-cell collection

Fresh tumor and adjacent liver tissue were collected and processed shortly after 690 surgery. The invasive margin was separated from the tumor center using a scalpel. All three regions were individually cut into small pieces and transferred into 2.5 ml of digestion medium per 0.5 g of tissue. The digestion medium consisted of RPMI-1640 medium (Thermo Fisher Scientific, #31870-025) supplemented with 10% fetal bovine serum (FBS; Thermo Fisher Scientific, #A5209402), 1 mg/ml Collagenases IV 695 (Worthington, #LS004191), and 0.25mg/ml DNase I (Sigma-Aldrich, #DN25-5G). Tissues were enzymatically digested in a 6-well plate for 1 hour at 37°C with constant shaking at 90 rpm. The digestion was stopped with cold PBS containing 2 mM of EDTA (VWR chemicals, #E177). The digested tissue was filtered through a 100 µm cell strainer (Chemie Brunschwig, #7002109), and the resulting cell suspension was 700 centrifuged at 300 g for 10 minutes at 4°C. The supernatant was discarded, and the pelleted cells were suspended in debris removal solution (Miltenyi Biotec, #130-109-398) accordingly to manufacturer's instructions. In some experiment, red erythrocytes

were removed by incubation with red blood cell lysis buffer (abcam, #ab204733) for 3 minutes at room temperature. After washing, the cells were counted and resuspended in FBS containing 10% of DMSO (Applichem Panreac, #A3672.0050). The cell suspensions were aliquoted into freezing tubes (Nunc CryoTube, Thermo Fisher Scientific #366656) and placed in a CoolCell Cell Freezing container (Corning) at -80°C. After at least 24 hours, the vials were transferred to liquid nitrogen for long-term storage.

Staining for Flow cytometry

Fresh frozen vials of cell suspensions from patient samples listed (Figure S1A) were thawed by centrifugation at 350g for 7 min at 21°C in a 15mL falcon tube containing warm complete medium with 4 U/mL of benzonase (Merck, #70746-3). Complete medium consisted of RPMI-1640 medium (Thermo Fisher Scientific, #31870-025) supplemented with 5% of FBS (Thermo Fisher Scientific, #A5209402), 100 U/mL of Penicillin-Streptomycin (Thermo Fisher Scientific, #15140122), 2mM of L-Glutamine (Thermo Fisher Scientific, #25030024). Cell pellets were resuspended in complete medium containing 2 U/mL of benzonase and counted to ensure no more than 1.5 million cells were stained per sample to minimize variability between samples. The cells were transferred to a 96-well V-bottom plate, and staining was performed after washing the medium with PBS. Cell pellets were resuspended in 50 uL per well of PBS containing Zombie NIR Fixable Dye (Biolegend, #423106, dilution 1/600), Fc Receptor Blocking Solution (Biolegend, #422302, dilution 1/200), and True-Stain Monocyte Blocker (Biolegend, #426102, dilution 1/100), followed by incubation for 20 minutes at 4°C. After washing with PBS and centrifugation at 450g for 5 minutes, the supernatant was removed. Next, 50uL of RPMI-1640 medium supplemented with 3% of FBS at room temperature containing the antibody targeting chemokine receptor (CXCR6, CCR7, CX3CR1) was added, and the mixture was incubated for 15 minutes at 37°C. Subsequently, 50 uL of cold RPMI-1640 medium supplemented with 3% of FBS containing all remaining antibodies targeting extracellular proteins were added on top of each well and incubated for additional 30 minutes on ice. After washing with PBS and centrifuging at 450g for 5 minutes, the supernatant was removed. Fixation/Permeabilization buffer (Thermo Fisher Scientific, #00-5523-00; 150uL per well) was added and incubated for 35 minutes on ice. After centrifugation at 600g for 7 minutes, the supernatant was discareded. Next, 50uL of Permeabilization buffer (Thermo Fisher Scientific, #00-5523-00) containing antibodies targeting intracellular proteins (CTLA-4, EOMES, T-bet, Ki67, FoxP3 and TOX) was added to each well and incubated overnight at 4°C. The following morning, 50uL of Permeabilization buffer containing anti-TCF-1, anti-Granzyme B and streptavidin antibodies was added to each well and incubated for 35 minutes at 4°C. After a final wash with Permeabilzation buffer and centrifugation at 600g for 5 minutes, the supernatant was removed. The cells were resuspended in 100uL of PBS, and the acquisition was performed on the Cytek Aurora 5-laser flow cytometer and data were collected as FCS files. All antibodies used are listed in the STAR★Methods and in Table S1.

Rhapsody experiment

750 Fresh frozen vials of cell suspensions from patient samples listed (Figure S7A) were thawed by centrifugation at 250 g for 10 minutes at 21°C in a 15 mL Falcon tube containing warm complete medium. The complete medium consisted of RPMI-1640 medium (Thermo Fisher Scientific, #31870-025) supplemented with 10% FBS (Thermo Fisher Scientific, #A5670402). Cell pellets were resuspended in complete 755 medium, transferred to FACS tubes, and centrifuged again. Cell pellets were resuspended in 100 µL of labeling buffer containing Zombie NIR Fixable Dye (BioLegend, #423106, dilution 1:600) and Fc Receptor Blocking Solution (BioLegend, #422302, dilution 1:200) and incubated for 10 minutes on ice. The labeling buffer consisted of PBS supplemented with 3% FBS and 0.1 g/L herring sperm DNA (Thermo 760 Fisher Scientific, #15634-017). Next, 80 µL of labeling buffer containing anti-CD45 BV785, anti-CD38 BV650, anti-CD14 FITC (final dilution 1:100), anti-CD19 SuperBright 436 (final dilution 1:50), and anti-KLRG1 APC (final dilution 1:200) was added along with 20 µL of Sample Tag (BD Biosciences, #633781). After 30 minutes of incubation on ice, cells were washed with washing buffer (PBS supplemented with 765 3% FBS), centrifuged, and resuspended in sorting buffer. Sorting buffer consisted of HBSS (Thermo Fisher Scientific, #14175095) supplemented with 10% FBS and 10 mM HEPES (Thermo Fisher Scientific, #15630080). Cells were sorted as CD45-positive, live cells, SSC-A low, CD14-negative, CD19-negative using a BD FACSymphony™ S6 Cell Sorter with a 100 µm nozzle, sample agitation set at 300, 4-770 way purity, and maintained at 4°C. The sorted cells were pooled according to their sample tag index. After sorting, cells were centrifuged and resuspended in 100 µL of labeling buffer, to which 100 µL of AbSeq antibody mix was added. This mix contained pre-titrated AbSeq antibodies from the Discovery Panel (BD Biosciences, #625970) along with 14 additional AbSeq antibodies at 1:200 dilution, as detailed in the 775 STAR★Methods and Table S2. After two washes with PBS and one with sample buffer (BD Biosciences, #650000062), cells were resuspended in sample buffer, counted, and the cell concentration was adjusted to load no more than 50,000 cells per cartridge. Single-cell capture was performed according to the manufacturer's instructions (BD Biosciences, Doc ID: 210967 Rev. 3.0). cDNA synthesis and template 780 switching were carried out following the manufacturer's instructions (BD Biosciences, Doc ID: 23-24020(03)). Library preparation from the beads was performed by the Functional Genomics Center Zurich, following the manufacturer's instructions (BD Biosciences, Doc ID: 23-24020(03)). Sequencing was performed on the Illumina NovaSeq 6000 platform, with the following read configurations: 40,000 reads for whole 785 transcriptome mRNA analysis, 1,000 reads for sample tags, 5,000 reads for TCR, and 25,000 reads for AbSeq. All antibodies and reagents used are listed in the STAR★Methods and Table S2.

Ex vivo stimulation

790

Fresh frozen vials of cell suspensions from the patient samples listed (Figure S8A) were thawed by centrifugation at 250 g for 10 minutes at 21°C in a 15 mL Falcon tube containing warm complete medium. The complete medium consisted of RPMI-1640 medium (Thermo Fisher Scientific, #31870-025) supplemented with 10% FBS (Thermo Fisher Scientific, #A5670402). Cell pellets were resuspended in 100 µL of live-dead labeling buffer containing Zombie NIR Fixable Dye (BioLegend, #423106, dilution 1:600) and Fc Receptor Blocking Solution (BioLegend, #422302, dilution 1:200) and incubated for 10 minutes on ice. The labeling buffer consisted of PBS supplemented with 3% FBS. Next, 100 µL of labeling buffer containing anti-CD45 PerCP, anti-CD3 BUV805, anti-CD4 Spark Blue 550, anti-CD8 PE, anti-CD56 PE-Dazzle594, anti-CD25 R718, anti-CD45RO PE-Cy7, CD161 BV785, CD127 BV605, CD103 BV510, and CD69 BV421 (information on clones and dilutions in Table S3) were added to the well and incubated for 30 minutes on ice. After washing, cells were sorted as indicated (Figure S8B) using a BD FACSymphony™ S6 Cell Sorter with a 100 µm nozzle, sample agitation set to 300, 4-way purity, and maintained at 4°C.

Beforehand, 96-well plates (Sarstedt, #7510036) were prepared by coating with 0.5 µg/mL anti-CD3 antibody (clone OKT3, ThermoFisher Scientific, #16-0037-85) alone or combined with 1 µg/mL of Recombinant Human CD40-Fc Chimera recombinant protein (Biolegend, #777202) or anti-CD28 antibody (clone CD28.2, ThermoFisher Scientific, #16-0289-85). Each well was coated with 100 µL of PBS containing the antibody and incubated either for 2 hours at 37°C or overnight at 4°C, followed by three washes. After sorting, cells were centrifuged and resuspended in DMEM supplemented with 10% FBS, sodium pyruvate (1mM, ThermoFisher Scientific, #11360070), MEM Non-Essential Amina Acids (1X, ThermoFisher Scientific, #11140050), L-glutamine (2mM, ThermoFisher Scientific, #25030081), β-mercaptoethanol (AppliChem GmbH, # A1108,0100), and penicillin/streptomycin (Gibco, #7001592) to a concentration of 1 million cells/mL, based on the sorter count. After resting for 2 hours at 37°C, cells were counted, and the concentration was adjusted to load 30,000 cells in 100uL per well into the prepared 96-well plate Ab-coated. After 48 hours of incubation, cells were centrifuged, and the supernatant was stored at -80°C for LEGENDplex analysis. The cells were transferred to a V-bottom 96-well plate for activation marker staining.

Cells were stained with 50 µL of live-dead labeling buffer for 10 minutes on ice. Then, 50 µL of an antibody mix (anti-CD45 PerCP, anti-CD3 BUV805, anti-CD25 PE, CD69 BV421, CD27 BUV563, PD-1 BV605, CD28 BV750, TIM3 FITC, CD38 APC-Fire 810, HLA-DR BUV395) was added to the cell suspension and incubated for an additional 30 minutes at 4°C. Fixation/Permeabilization buffer (Thermo Fisher Scientific, #00-5523-00; 100 µL per well) was added and incubated for 35 minutes on ice. After washing, 100 µL of Permeabilization buffer (Thermo Fisher Scientific, #00-5523-00) containing antibodies targeting intracellular proteins (T-bet BV711, CD40L AF647, Granzyme B AF700, Granzyme K PE-Cy7, Ki67 BV480) was added to each well and incubated overnight at 4°C. The following morning, cells were washed with Permeabilization buffer and acquired on the Cytek Aurora 5-laser flow cytometer. All

antibodies used are listed in the STAR★Methods and Table S3. Cytokine measurement from the undiluted supernatant was performed using the LEGENDplex™ HU Th Cytokine Panel (12-plex, #741028, BioLegend) following the manufacturer's instructions. Analysis was performed using the LEGENDplex data analysis software.

Multiplex imaging on tissue microarrays

FFPE samples from the cohort in Figure S1A were H&E-stained, scanned, and a board-certified pathologist (B.S.) selected 600 µm tissue cores, five cores from each the tumor center and invasive margin compartment (as defined [80]), and three from perilesional normal tissue, for construction of tissue microarrays (TMAs) using the TMA Grand Master (3D Histech). Sections of 2 µm were mounted on glass slides for re-evaluation and confirmation of region annotations. Of 390 cores, 17 were reclassified from tumor center to invasive margin, 13 from invasive margin to tumor center, and 80 were excluded due to disruption or uncertain regional assignment.

Sequential immunofluorescence imaging was performed using the COMET™ platform (Lunaphore Technologies) using a 18-protein panel + DAPI. All antibodies used are listed in the STAR★Methods and Table S4. Slides with FFPE tissue were pre-processed using the PreTreatment Module (PTM) and Deparaffinization and heat-induced epitope restrieval solution from Epredia™ for the dewaxing and antigen-retrieval protocol (pH=9, Temperature= 102°C) performed on slides before the staining on COMET™ as recommended by Lunaphore Technologies. The slides were then loaded onto the COMET™ Stainer and processed according to manufacturer's recommendations. Samples underwent iterative staining with primary antibodies, secondary antibodies, and subsequent imaging, followed by elution of the primary and secondary antibodies, and imaging of residual background, as previously described [48]. All primary antibody incubations were performed for 4 to 8 minutes. The platform automatically processes the individual fields of view from each cycle, overlays, align and stitches them, resulting in a large multi-layer ome.tiff images file. Lunaphore Viewer was used to view the images and remove background fluorescence. QuPath 0.6.0-rc3 was used to define the TMA grid with the TMA dearrayer, identify and annotate disrupted regions, and perform cell segmentation using Instanseg [81], an embedding-based instance segmentation algorithm that uses DAPI and specified markers signals (CD3, CD20, CD11c, CD68 and CD56). After segmentation, each cell's x and y coordinates and the median fluorescence signals from the nucleus and cell were exported for downstream R analysis.

Analysis Flow Cytometry

After correction of the compensation matrix using FlowJo software (version 10.9.0), cells were gated on single, live immune cells (gating strategy shown in Figure S6A, up to "Cleaned CD45+"). Cleaned cells were exported as new FCS files and imported into

880 R version 4.4.1 for analysis. Before automated high-dimensional data analysis, flow cytometry data were transformed using an inverse hyperbolic sine (arcsinh) function with a manually determined cofactor and normalized between 0 and 1 (Table S5). A preliminary round of unsupervised clustering using FlowSOM (version 2.12.0) was conducted to clean the data and exclude non-lymphocyte cells from downstream
885 analysis. Signal alignment for each marker across samples was checked. Samples with fewer than 1,000 cells were excluded from the analysis. For clustering of major lymphoid cells, UMAP was generated using 1,000 cells per sample and all markers except TIGIT, CD45, Live/Dead, and CD14. FlowSOM clustering was performed using CD3, CD4, CD8, CD161, CD45RO, CD127, CXCR6, CD56, KLRG1, TCRγδ, CD16,
890 FoxP3, and CX3CR1 to identify 11 clusters. These clusters were subsequently merged based on marker expression into the following categories: Treg, CD4 T cells, CD8 T cells, MAIT, DP T cells, DN T cells, NK cells, TCRγδ T cells, and B cells.

For subsequent clustering of CD4 T cells, the previously identified major lymphoid
895 CD4 T cell and Treg clusters were combined for downstream analysis. UMAP was generated using 1,000 cells per sample when possible. For UMAP and FlowSOM clustering, 24 markers were used, corresponding to all markers except TIGIT, CD45, Live/Dead, CD14, CD3, CD4, CD19, CD16, and TCRγδ. A total of 21 clusters were identified and merged based on marker expression into the following subsets: Naive,
900 CM, Mem1, Mem2, RM, Mem CD161, SLEC, Effector, Effector PD1high, Tpex, Tex Term, Tex Prolif, T Prolif, and Treg. For subsequent clustering of CD8 T cells, UMAP was generated using 1,000 cells per sample when possible. For UMAP and FlowSOM clustering, 23 markers were used, corresponding to all markers except TIGIT, CD45, Live/Dead, CD14, CD3, CD4, CD8, CD19, CD16, and TCRγδ. A total of 10 clusters
905 were identified and merged based on marker expression into the following subsets: Tex Term, RM, Tex Transitory, Innate-like, TEMRAs, SLEC, Effector, Mem, and Prolif. Subsequent analyses of all identified clusters were performed by merging the detailed CD4 and CD8 T cell clustering with other major lymphocyte populations, including NK cells, TCRγδ T cells, MAIT cells, DP T cells, DN T cells, and B cells.
910

Radar plots were generated using the *fmsb package* (version 0.7.6): For the phenotype of all 29 immune subsets identified in the merged analysis (Figure S2B and Figure S3B), the axis limits for the radar plots are based on the minimum and maximum median values for each of the 29 lymphocyte markers across all 29 immune
915 subsets. For the ex vivo stimulation (Figure 5B and S5E), the radar plots were generated using the median fluorescence intensity. The axis limits for the radar plots are based on the minimum and maximum median values for each marker, determined across all groups (CD4 Mem1, CD4 Mem2, CD8 Mem, and CD8 EM) and under all stimulation conditions (unstimulated, aCD3/CD40, and aCD3/aCD28).
920 For the 10 closest neighborhood spatial analysis (Figure 6C and Figure S11B), radar plots show the mean cell type composition of CD4 or CD8 neighborhoods in the invasive margin and tumor center per response group. The radial axis of the radar plot is scaled to a maximum of 35%.

925 PCA analysis was performed using the *stats package* (version 4.4.1) to evaluate landscape changes by region based on the frequency of all 29 clusters across the 76 samples collected from all patients and grouped by region: 27 samples from the tumor center, 25 from the invasive margin, and 24 from the perilesional normal tissue (Figure S4C-D). To assess phenotypic changes by region, PCA analysis was performed on
930 the median fluorescence intensity (MFI) of the 29 lymphocyte markers. As PCA analysis cannot handle NA values, clusters CD4 Tex Term, CD4 Tpex, and CD4 Tex Prolif, which were absent from several patients, were excluded. Additionally, the tumor center sample from patients 1 and 29, the invasive margin sample from patient 12, and the perilesional normal sample from patient 25, which were missing additional
935 clusters, were removed. This analysis was performed on 26 immune subsets and a total of 25 samples from the tumor center, 24 from the invasive margin, and 23 from the perilesional normal tissue (Figure S4E-F). Finally, to evaluate changes in the immune landscape in response to NAC, PCA analysis was conducted by region based on immune subset frequency and grouped by TRG. After filtering on patient from which
940 the TRG information was available, we depicted 22 patients in the tumor center (10 with TRG 4&5, 6 with TRG 3, and 6 with TRG 1&2), 21 patients in the invasive margin (10 with TRG 4&5, 6 with TRG 3, and 5 with TRG 1&2), and 20 patients in the perilesional normal tissue (11 with TRG 4&5, 4 with TRG 3, and 5 with TRG 1&2), grouped by TRG (Figure 3E-F and Figure S5C-D).
945

Module analysis

To interrogate the immune microenvironment, we examined co-enrichment patterns across the 29 identified lymphoid clusters from the 76 samples. Spearman correlations
950 between lymphoid subset frequencies across all samples were calculated, followed by hierarchical clustering, which identified three distinct cell modules with coordinated behavior.

To calculate the abundance of each module, we performed the following steps:

1. Equal weighting for each cell type was ensured by normalizing the frequency
955 of each cluster per sample between 0 and 1 to the 1st–99th percentile.
2. Module scores were calculated as the mean frequency of all immune subsets within each module (i.e., sum of frequencies divided by the number of cell types per module). This ensured that scores ranged from 0 to 1, giving equal importance to each module regardless of size.
960 3. The module with the highest score was identified as the most abundant module per sample.
4. The scores were transformed into percentages representing the abundance of each module per patient. This normalization ensured that the sum of module abundances for each patient equaled 100%.
965 5. Module abundance was evaluated across all samples by region.

Notably, module analysis was also performed within the tumor center, and metastatic module abundance was evaluated by TRG. For this analysis, tumor center samples were filtered, and the module analysis was repeated following the same steps as

above. However, the frequencies of each lymphocyte subset were not normalized again, preserving the coherence of the general composition per region.

Rhapsody analysis

Data processing, QC and cleaning

The BD Rhapsody Sequence Analysis v1.12.1 pipeline was used to align reads to the human reference genome (Build GRCh38.p13 with gene model definition from GENCODE, release 37) and generate the gene-cell unique molecular identifier (UMI)-adjusted matrix (RSEC) for each sample. The obtained raw count matrix was loaded into the Seurat workflow (version 5.1.0) for downstream analyses. Genes detected in fewer than three cells in each cartridge were filtered out prior to analysis. Quality control (QC) of cells was performed using three sequential metrics: total counts, the number of detected genes, and the proportion of mitochondrial gene counts per cell. Cells with mitochondrial gene expression exceeding 24% were excluded, as well as cells with fewer than 800 detected genes. To eliminate potential doublets, cells with total counts over 15,000 and detected genes exceeding 4,000 were also removed. For multiplexing, following expert recommendations from the BD Rhapsody platform, multiplets were recalled when a tag represented more than 75% of the total tag reads. After QC, the data matrix was normalized to 10,000 counts per cell using *Seurat::NormalizeData()* function, ensuring comparability among cells. The normalized counts were log-transformed as part of this process, and data scaling was performed using *Seurat::ScaleData()* function. Highly variable genes were identified using the *Seurat::FindVariableFeatures()* function with the variance-stabilizing transformation (VST) method, selecting the top 2,000 most variable genes for downstream analysis. Principal Component Analysis (PCA) was performed on these highly variable genes using the *Seurat::RunPCA()* function. A shared nearest neighbor (SNN) graph was constructed using *Seurat::FindNeighbors()* function, based on the first 13 PCs from the PCA space. Cells were clustered into distinct groups using *Seurat::FindClusters()* function, employing the Louvain algorithm. Based on mRNA clustering, four clusters that were not pure NK or T cells were removed from subsequent analyses. For Antibody-Derived Tag (ADT) data, variable features were defined using all features within the ADT assay. Normalization was performed using the Centered Log Ratio (CLR) transformation with *Seurat::NormalizeData()* function, normalizing across features (margin = 2). The normalized data were scaled using *Seurat::ScaleData()*, and PCA was performed with *Seurat::RunPCA()* function. Using the first 10 PCs, an SNN graph was constructed with *Seurat::FindNeighbors()* function, and clustering was conducted using *Seurat::FindClusters().* Clusters with inconsistent staining, reflecting potential doublets, and clusters that did not represent NK or T cells were removed from the analysis.

Identification of CD4 and CD8 T cell

For downstream analysis, both the RNA and ADT assays were normalized and scaled again and the cleaned data, as described before. As each patient were received in different days and the three regions were processed independently, the RNA data set

1015 was corrected for batch effects and integrate across patients using harmony integration [41]. This was performed using *Seurat::RunHarmony()* function (lambda = 1.5 and theta = 3). Fourteen harmony clusters were identified based on RNA clustering analysis using the first 12 PC and a resolution of 0.9. Similarly, the ADT data set was corrected for batch effects and integrated using Seurat's anchoring method [82].
1020 Features such as CD14, CD19, IgD, and IgM were excluded due to their lack of relevance. Integration anchors were identified using the *Seurat::FindIntegrationAnchors()* function. The datasets were integrated using the *Seurat::IntegrateData()* function, and the resulting integrated assay was stored as IADT in the original dataset. Five major populations were identified based on IADT
1025 clustering analysis, utilizing CD3, CD8, CD56, CD4, CD161, KLRG1, CD127, CD45RO, and TCRγδ as protein markers for clustering, with a resolution of 0.2. The identified populations were CD4 T cells, CD8 T cells, NK cells, TCRγδ T cells, and MAIT cells. To study CD4 and CD8 T cells separately, we implemented a multistep filtering process. First, CD4 and CD8 T cells were identified based on clusters in the
1030 integrated proteomic dataset (IADT). To refine these clusters, we reassigned CD4 Treg cells identified from the integrated RNA clustering analysis to the CD4 T cell population, excluding any CD8 T cells and ensuring that all Treg were identified. Finally, clusters corresponding to MAIT cells, NK cells, and stressed cells, as identified from the integrated RNA clustering analysis, were excluded from both the CD4 and
1035 CD8 T cell populations.

Analysis CD4 and CD8 T cell

Both CD4 and CD8 T cell RNA data set were scaled again and the proteomic IADT and transcriptomic harmony integrated modalities were integrated using the Weighted
1040 Nearest Neighbor (WNN) workflow [83] using *Seurat::FindMultiModalNeighbors()* function with PC 13 of the harmony RNA and PC 10 of the IADT. For CD4 T cells, resolution 0.5 was used to identify 10 clusters, two clusters were merged as Mem1 and two as Treg; while for CD8 T cells, resolution 0.4 was used to identify 8 clusters. For visualization, the dimensionality was further reduced using UMAP implemented in
1045 the *Seurat::RunUMAP()* function. Differentially expressed genes were identified using the *Seurat::FindAllMarkers()* function, reporting only genes with positive log fold change, a minimum detection rate of 25%, and a log fold change threshold of 0.25 (Table S6, Table S7). Rhapsody signature of each subset was defined by filtering differentially expressed genes that are detected in more than 30% of cells in the target
1050 cluster (pct.1 > 0.3), less than 30% of cells in other clusters (pct.2 < 0.3), and if their average log2 fold change (avg_log2FC) exceeded 0.3 (Table S8).

Signatures z-score were calculated using the function *Seurat::AddModuleScore()* using list of genes from previously described signatures: stem-like memory signature
1055 [66] for CD8 T cells and (Cardenas et al., 2024)(Cardenas et al., 2024) for CD4 T cells, circulating memory and residency T cell signatures (Kumar et al., 2017)(Kumar et al., 2017), cytotoxic CD8 (Jerby-Arnon et al., 2018)(Jerby-Arnon et al., 2018) T cells signatures, and MSigDB signatures for TGFb, Hypoxia. Th1 and Th17 signatures were defined using curated gene sets, with Th17 characterized by AHR, CCR6, TGFB1,

1060 REL, RELA, IL23R, CCL20, CEBPD, STAT3, STAT4, and IL23A; and Th1 defined by IFNG, XCL1, TBX21, CCL4, CCL5, CCL3, CSF2, IL2, STAT1, CXCR3, and TNF.

Single-cell regulatory network inference and clustering (SCENIC) on CD4 T cells was performed using the pySCENIC workflow [37]. Genes expressed in less than 0.5% of
1065 cells were filtered out, and the rest was performed with standard parameters. The reference files used were allTFs_hg38, hg19-tss-centered-10kb-7species.mc9nr.genes_vs_motifs.rankings.feather and motifs-v9-nr.hgnc-m0.001-o0.0.tbl, downloaded from the aertslab resources cistarget databases and motif2tf.

1070 TCR sequencing data were analyzed using the scRepertoire (v2.2.1) workflow [86] and merging all cluster from the CD4 and CD8 T cell analysis with WNN workflow clustering. We used the *clonalBias()* function [87] to assess clonal skewing across clusters by patient and calculating baseline frequencies with a minimum expansion threshold of five. We used the *clonalOverlap()* function with the "morisita" method to
1075 evaluate and visualize the similarity of TCR clonotypes across clusters.

Data mining Liu et al., 2022

The data set from Liu et al., 2022 [29] was downloaded and included 10 patients with
1080 CRLM, who had not undergone NAC treatment. We used the major annotation from the original dataset to extract the CD4 T cell cluster, comprising 13,416 cells from the tumor center tissue (metastatic tumor) and 4,551 cells from the perilesional normal tissue (metastatic normal). Harmony was used to integrate this dataset with the CD4 T cells from our dataset, which included 15,470 cells, to correct for both batch effects
1085 and patient effects, as the samples were processed independently. This integration was performed using *Seurat::RunHarmony()* function (lambda = 1.5, theta = c(3,3)) on the variable features from the Rhapsody data. Seven clusters were identified after integration, based on RNA clustering analysis using the first 12 PCs and a resolution of 0.4. Similarly, we used the major annotation from the original dataset to extract the
1090 CD8 T cell cluster, which included 7,198 cells from the tumor center tissue (metastatic tumor) and 15,248 cells from the perilesional normal tissue (metastatic normal). Harmony was used again the same parameters than before, to integrate this dataset with the CD8 T cells from our dataset, containing 19,767 cells, to correct for both batch effects and patient effects, as the samples were processed independently. Nine
1095 integrated clusters were identified based on RNA clustering analysis using the first 12 PCs and a resolution of 0.5.

For visualization, dimensionality was further reduced using UMAP, implemented with the *Seurat::RunUMAP()* function. Signature z-scores were calculated using the
1100 *Seurat::AddModuleScore()* function, with gene lists from the previously described Rhapsody signature.

Data mining Wu et al., 2022

1105 The data set from Wu et al., 2022 [43] was downloaded and included 20 patients with CRC Stage IV: 11 with CRLM and no treatment (pretreated, 21,423 cells), six patients treated with NAC with progressive disease or stable disease (treated-PD/SD, 7,167 cells), and three patients treated with NAC with partial response (treated-PR, 20,671 cells). The raw count matrix was loaded into the Seurat workflow for downstream
1110 analyses. Quality control (QC) of cells was performed using three sequential metrics: total counts, the number of detected genes, and the proportion of mitochondrial gene counts per cell. Cells with mitochondrial gene expression exceeding 10% were excluded, as were cells with fewer than 400 detected genes. To eliminate potential doublets, cells with total counts over 15,000 and detected genes exceeding 3,000
1115 were also removed. Batch effect per patient sample was correct using *Seurat::RunHarmony()* function (lambda = 1.5, theta = 3).
We identified sixteen clusters based on RNA clustering analysis using the first 12 PCs and a resolution of 0.9. Six of these clusters were identified as CD4 T cells, including Tregs, and were reclustered following the previously described method. After re-
1120 clustering on CD4 T cells using the first 10 PCs and a resolution of 0.4, we identified six clusters. For visualization, dimensionality was further reduced using UMAP, implemented with the *Seurat::RunUMAP()* function. Signature z-scores were calculated using the *Seurat::AddModuleScore()* function with the following gene lists:

- Circulating, less differentiated memory: S1PR1, CCR7, KLF3, CD55
- 1125 Tissue Th1-like: CD69, IFNG, CD40LG, TNF, TBX21
- Th17-like: KLRB1, AHR, CCL20, IL23R
- Suppressive Treg: FOXP3, IL2RA, CCR8, IL1R1

1130 Analysis of Multiplex-imaging

Before automated high-dimensional data analysis, multiplex-imaging data were transformed using an inverse hyperbolic sine (arcsinh) function with a manually determined cofactor (Table S9) and normalized between 0 and 1. Batch correction
1135 between the four slides of TMAs was performed using cyCombine algorithm [88] with batch as slide and considering the region (tumor center, invasive margin and perilesional normal tissue) as covariable. A preliminary round of unsupervised clustering using FlowSOM (version 2.12.0) was conducted to clean the data from artefact and exclude unstained cells (CD3, HLA-DR, CD4, CD56, CD8, CD11c, CD68,
1140 CD20, SATB2, PanCK, CD69, CD11b) from downstream analysis. The resulting cells were first annotated as immune cells (expressing CD3, CD4, CD56, CD8, CD20, HLA-DR, CD11c, CD68 or CD11b), non-tumor epithelial cells (expressing PanCK but SATB2 negative), cholangiocytes (expressing PanCK and CD56) or tumor cells (expressing both PanCK and SATB2) using 15 clusters from FlowSOM clustering
1145 based on the previously mentioned markers. For subsequent clustering, the data for the immune cells were transformed and batch corrected again as previously described and in order to improve the signal separation on this compartment and cells with the DAPI nucleus signal lower than 250 or an area lower than 15µm^2 were filtered out. Immune cells were then subclustered using CD3, CD4, CD56, CD8 and CD20 for

1150 FlowSOM to identify 7 clusters which were merged into the following categories: T cells, B cells, Myeloid cells and NK cells. T cells were then subclustered with FlowsSOM to ientify 4 clusters namely CD4 T cells, CD8 T cells, other T cells ($CD3^+$ $CD4^-$ $CD8^-$) and Tregs. The identification of Treg cells was optimized by considering CD4 T cells with FOXP3 signal higher than 0.25, CD4 signal higher than 0.15 and
1155 CD8 signal lower than 0.35. Finally, CD4 T cells were subclustered using TCF1, Ki67, CD69 and PD-1 to identify 15 clusters merged into CD4 Tex Term ($TCF1^-$ $PD1^+$), CD4 Tpex ($TCF1^+$ $PD\text{-}1^+$), CD4 prolif ($Ki67^+$), CD4 $TCF1^+$ $CD69^-$, CD4 $TCF1^+$ $CD69^+$, CD4 $TCF1^-$ $CD69^+$ and CD4 $TCF1^-$ $CD69^-$. CD8 T cells were subclustered using TCF1, Ki67, GzmK and PD-1 to identify 18 clusters merged into CD8 Tex Term ($TCF1^-$ $PD1^+$),
1160 CD8 prolif ($Ki67^+$), CD8 $TCF1^+$ $GzmK^-$, CD8 $TCF1^+$ $GzmK^+$, CD8 $TCF1^-$ $GzmK^+$ and CD8 $TCF1^-$ $GzmK^-$. Myeloid cells were subclusterd using CD68, HLA-DR, CD11c, CD11b to identify 9 clusters merged into DCs ($CD68^-$ $HLA\text{-}DR^+$ $CD11c^+$), Macrophages ($CD68^+$) $HLA\text{-}DR^+$ $CD11c^+$ or $HLA\text{-}DR^+$ $CD11c^-$ and myeloid $CD11b^+$ $HLA\text{-}DR^+$ or $CD11b^+$ $HLA\text{-}DR^-$. UMAP was generated using all the annotated cells
1165 (408'311) based on CD3, HLA-DR, CD4, CD56, CD8, CD11c, CD68, CD20, SATB2, PanCK, FOXP3, CD11b. Density of the different subsets was calculated by dividing the sum of cell count of all TMAs collected by the sum of the area (mm^2), for each patient and region. The area was calculated considering that each TMA cores consist of a 600 µm diameter punch (area ≈ 0.283 mm^2) from which we subtracted areas being
1170 annotated as disrupted.

To investigate spatial interactions between immune cell populations, we calculated pairwise Euclidean distances between all cells within each individual TMA core. For downstream quantification, we filtered for distance occurring within a 15 µm threshold,
1175 representing putative physical proximity for cell–cell communication. For each TMA punch, we computed the number of close-range cell–cell proximities for all cell type pairs, we generated all possible combinations of cell type pairs across all TMA punches and filled in zero values for missing combinations. Interaction counts were normalized to the segmented tissue area (yielding a density of interactions per mm^2)
1180 for each patient and region. The median interaction density for responder and non-responder is displayed.

Neighborhood analysis of CD4 T cells in CRLM tissues was performed by retrieving the 10 closest non-CD4 T cell neighbors to each CD4 T cell. For each patient and
1185 region, we computed the neighbor cell type composition and summarized each response group by the mean proportion. For visualization, we showed the profiles in a radar plot (fmsb::radarchart) for responders (TRG1&2) and non-responders (TRG4&5), with a radial axis to a maximum of 35%. Neighborhood analysis of CD8 T cells in CRLM tissues was performed in the same manner, retaining the 10 closest
1190 non-CD8 T cell neighbors to each CD8 T cell.
The proximity score was calculated as the ratio of identified interactions (using a 15 µm radius threshold to CD4 or CD8 T cells) to the total number of cells of the interacting type, providing insight into how frequently these cell type interacts relative

to their population size [89]. Scores were averaged across blocks within the same responder group.

To identify spatially proximate immune cell triads We built an undirected proximity network per sample and region from all cell pairs with Euclidean distance 0<d<15µm. We identified fully connected subgraphs (cliques) of size ≥3 and retained only those containing at least one CD4 T cell, one stem-like CD8 T cell (TCF1$^+$ GzmK$^+$ or TCF1$^+$ GzmK$^-$), and one antigen-presenting cell (B cells, dendritic cells, macrophages HLA-DR$^+$ CD11c$^+$, macrophages HLA-DR$^+$, or myeloid CD11b$^+$ HLA-DR$^+$). We then counted the number of cells participating in at least one qualifying triad and normalized by the segmented tissue area to report cells-in-triads per mm². Finally, for APC-type in triad, we computed the density of APC triad members per subset and summarized these per-subset densities by response group using the mean across patients.

Statistical analysis

In the Flow Cytometry analysis, the Rhapsody, the data mining analyses and the multiplex-analysis, statistical significance in frequency or density was determined using paired (when comparing regions) or unpaired (when comparing response group) Wilcoxon tests corrected for multiple comparisons using the Benjamini-Hochberg method. The analysis was conducted in R with the *compare_means()* function from the ggpubr package (version 0.6.0). Significance levels are displayed as follows, * pvalue adjusted <0.05, ** pvalue adjusted <0.01, *** pvalue adjusted < 0.001,**** pvalue adjusted <0.0001. We calculated the effect size of changes of MFI using Cohen's d, the calculation was performed in R using the effsize package (version 0.8.1), specifically the *cohen.d()* function

Spearman correlation test was used to measure the strength and direction of the frequency of each immune subset to the TRG. A positive Spearman correlation coefficient of Frequency vs TRG indicates an association with low TRG (i.e. responders), while a negative correlation indicates association with high TRG (i.e. non-responder). Significance levels are displayed as follows, * pvalue adjusted <0.05, ** pvalue adjusted <0.01, *** pvalue adjusted < 0.001,**** pvalue adjusted <0.0001.

For the scenic analysis, Wilcoxon rank-sum test was used to identify differentially active regulons between memory clusters (CD4 Mem1, CD4 Mem2 and CD4 Mem CD161). For each regulon with sufficient representation (more than 50 cells in the target cluster), the test compares the regulon activity values in the target cluster against the other clusters, calculating a p-value and log fold change for the difference in activity. The p-values are adjusted for multiple testing using the Benjamini-Hochberg (BH) method.

For statistical analysis of the 10 closest neighbor proportions between response groups (responder vs. non-responder, mid vs. non-responder, and responder vs. mid) in the multiplex imaging data, we used non-parametric permutation-based

independence tests (*independence_test()* function from the coin package (version 1.4.3)). P-values were corrected for multiple testing using the Benjamini–Hochberg method. Significance thresholds were indicated as follows: * pvalue adjusted <0.05, ** pvalue adjusted <0.01. Statistical testing for the proximity score, was performed separately for each neighbor type and region, an initial Kruskal–Wallis test was performed followed by Benjamini–Hochberg-adjusted pairwise Wilcoxon rank-sum tests for all group pairs (responder, mid, non-responder). Neighbor types were included only if each group contained at least two samples and neither group exhibited zero variance in scores.

Triad densities were compared by region across responder groups using Wilcoxon rank-sum tests stratified by anatomical region using the function (ggpubr::compare_means). Significance pvalue were reported as follows: * pvalue <0.05, ** pvalue <0.01, *** pvalue < 0.001. The APC-type in triad were compared using two sided Wilcoxon test with the function (stats::wilcox.test) applied within each combination of cluster, region, and responder group. Statistical significance was annotated as follows: * pvalue <0.05 and ** pvalue <0.01.

References

1. Sung, H., Ferlay, J., Siegel, R.L., Laversanne, M., Soerjomataram, I., Jemal, A., and Bray, F. (2021). Global Cancer Statistics 2020: GLOBOCAN Estimates of Incidence and Mortality Worldwide for 36 Cancers in 185 Countries. CA Cancer J Clin *71*, 209–249. https://doi.org/10.3322/caac.21660.
2. Gupta, R., Sinha, S., and Paul, R.N. (2018). The impact of microsatellite stability status in colorectal cancer. Curr Probl Cancer *42*, 548–559. https://doi.org/10.1016/j.currproblcancer.2018.06.010.
3. Hernandez Dominguez, O., Yilmaz, S., and Steele, S.R. (2023). Stage IV Colorectal Cancer Management and Treatment. J Clin Med *12*, 2072. https://doi.org/10.3390/jcm12052072.
4. Yu, J., Green, M.D., Li, S., Sun, Y., Journey, S.N., Choi, J.E., Rizvi, S.M., Qin, A., Waninger, J.J., Lang, X., et al. (2021). Liver metastasis restrains immunotherapy efficacy via macrophage-mediated T cell elimination. Nat Med *27*, 152–164. https://doi.org/10.1038/s41591-020-1131-x.
5. Lee, J.C., Mehdizadeh, S., Smith, J., Young, A., Mufazalov, I.A., Mowery, C.T., Daud, A., and Bluestone, J.A. (2020). Regulatory T cell control of systemic immunity and immunotherapy response in liver metastasis. Sci Immunol *5*. https://doi.org/10.1126/sciimmunol.aba0759.
6. Li, X., Ramadori, P., Pfister, D., Seehawer, M., Zender, L., and Heikenwalder, M. (2021). The immunological and metabolic landscape in primary and metastatic liver cancer. Nat Rev Cancer *21*, 541–557. https://doi.org/10.1038/s41568-021-00383-9.
7. Nordlinger, B., Sorbye, H., Glimelius, B., Poston, G.J., Schlag, P.M., Rougier, P., Bechstein, W.O., Primrose, J.N., Walpole, E.T., Finch-Jones, M., et al. (2013). Perioperative FOLFOX4 chemotherapy and surgery versus surgery alone for resectable liver metastases from colorectal cancer (EORTC 40983): Long-term results

of a randomised, controlled, phase 3 trial. Lancet Oncol *14*, 1208–1215. https://doi.org/10.1016/S1470-2045(13)70447-9.

8. Rubbia-Brandt, L., Giostra, E., Brezault, C., Roth, A.D., Andres, A., Audard, V., Sartoretti, P., Dousset, B., Majno, P.E., Soubrane, O., et al. (2007). Importance of histological tumor response assessment in predicting the outcome in patients with colorectal liver metastases treated with neo-adjuvant chemotherapy followed by liver surgery. Annals of Oncology *18*, 299–304. https://doi.org/10.1093/annonc/mdl386.
9. Viganò, L., Capussotti, L., De Rosa, G., De Saussure, W.O., Mentha, G., and Rubbia-Brandt, L. (2013). Liver resection for colorectal metastases after chemotherapy: Impact of chemotherapy-related liver injuries, pathological tumor response, and micrometastases on long-term survival. Ann Surg *258*, 731–742. https://doi.org/10.1097/SLA.0b013e3182a6183e.
10. Gruenberger, T., Arnold, D., and Rubbia-brandt, L. (2012). Pathologic response to bevacizumab-containing chemotherapy in patients with colorectal liver metastases and its correlation with survival. Surg Oncol *21*, 309–315. https://doi.org/10.1016/j.suronc.2012.07.003.
11. Wang, Y., Yuan, Y.-F., Lin, H.-C., Li, B.-K., Wang, F.-H., Wang, Z.-Q., Ding, P.-R., Chen, G., Wu, X.-J., Lu, Z.-H., et al. (2017). Pathologic response after preoperative therapy predicts prognosis of Chinese colorectal cancer patients with liver metastases. Chin J Cancer *36*, 1–11. https://doi.org/10.1186/s40880-017-0244-1.
12. Baldin, P., Van den Eynde, M., Mlecnik, B., Bindea, G., Beniuga, G., Carrasco, J., Haicheur, N., Marliot, F., Lafontaine, L., Fredriksen, T., et al. (2021). Prognostic assessment of resected colorectal liver metastases integrating pathological features, RAS mutation and Immunoscore. J Pathol Clin Res *7*, 27–41. https://doi.org/10.1002/cjp2.178.
13. Halama, N., Michel, S., Kloor, M., Zoernig, I., Benner, A., Spille, A., Pommerencke, T., Von Knebel Doeberitz, M., Folprecht, G., Luber, B., et al. (2011). Localization and density of immune cells in the invasive margin of human colorectal cancer liver metastases are prognostic for response to chemotherapy. Cancer Res *71*, 5670–5677. https://doi.org/10.1158/0008-5472.CAN-11-0268.
14. Wang, Y., Lin, H. cheng, Huang, M. yan, Shao, Q., Wang, Z. qiang, Wang, F. hua, Yuan, Y. fei, Li, B. kui, Wang, D. shen, Ding, P. rong, et al. (2018). The Immunoscore system predicts prognosis after liver metastasectomy in colorectal cancer liver metastases. Cancer Immunology, Immunotherapy *67*, 435–444. https://doi.org/10.1007/s00262-017-2094-8.
15. Mlecnik, B., Van Den Eynde, M., Bindea, G., Church, S.E., Vasaturo, A., Fredriksen, T., Lafontaine, L., Haicheur, N., Marliot, F., Debetancourt, D., et al. (2018). Comprehensive intrametastatic immune quantification and major impact of immunoscore on survival. J Natl Cancer Inst *110*, 97–108. https://doi.org/10.1093/jnci/djx123.
16. Van den Eynde, M., Mlecnik, B., Bindea, G., Fredriksen, T., Church, S.E., Lafontaine, L., Haicheur, N., Marliot, F., Angelova, M., Vasaturo, A., et al. (2018). The Link between the Multiverse of Immune Microenvironments in Metastases and the Survival of Colorectal Cancer Patients. Cancer Cell *34*, 1012-1026.e3. https://doi.org/10.1016/j.ccell.2018.11.003.

17. Giles, J.R., Globig, A.-M., Kaech, S.M., and Wherry, E.J. (2023). CD8+ T cells in the cancer-immunity cycle. Immunity *56*, 2231–2253. https://doi.org/10.1016/j.immuni.2023.09.005.
18. Waldman, A.D., Fritz, J.M., and Lenardo, M.J. (2020). A guide to cancer immunotherapy: from T cell basic science to clinical practice. Nat Rev Immunol *20*, 651–668. https://doi.org/10.1038/s41577-020-0306-5.
19. Bruni, D., Angell, H.K., and Galon, J. (2020). The immune contexture and Immunoscore in cancer prognosis and therapeutic efficacy. Nat Rev Cancer *20*, 662–680. https://doi.org/10.1038/s41568-020-0285-7.
20. Park, S.L., Gebhardt, T., and Mackay, L.K. (2019). Tissue-Resident Memory T Cells in Cancer Immunosurveillance. Preprint at Elsevier Ltd, https://doi.org/10.1016/j.it.2019.06.002 https://doi.org/10.1016/j.it.2019.06.002.
21. Galon, J., Costes, A., Sanchez-Cabo, F., Kirilovsky, A., Mlecnik, B., Lagorce-Pagès, C., Tosolini, M., Camus, M., Berger, A., Wind, P., et al. (2006). Type, Density, and Location of Immune Cells Within Human Colorectal Tumors Predict Clinical Outcome. Science (1979) *313*, 1960–1964. https://doi.org/10.1126/science.1129139.
22. Speiser, D.E., Chijioke, O., Schaeuble, K., and Münz, C. (2023). CD4+ T cells in cancer. Nat Cancer *4*, 317–329. https://doi.org/10.1038/s43018-023-00521-2.
23. Borst, J., Ahrends, T., Bąbała, N., Melief, C.J.M., and Kastenmüller, W. (2018). CD4+ T cell help in cancer immunology and immunotherapy. Nat Rev Immunol *18*, 635–647. https://doi.org/10.1038/s41577-018-0044-0.
24. Westcott, P.M.K., Sacks, N.J., Schenkel, J.M., Ely, Z.A., Smith, O., Hauck, H., Jaeger, A.M., Zhang, D., Backlund, C.M., Beytagh, M.C., et al. (2021). Low neoantigen expression and poor T-cell priming underlie early immune escape in colorectal cancer. Nat Cancer *2*, 1071–1085. https://doi.org/10.1038/s43018-021-00247-z.
25. Ho, W.W., Gomes-Santos, I.L., Aoki, S., Datta, M., Kawaguchi, K., Talele, N.P., Roberge, S., Ren, J., Liu, H., Chen, I.X., et al. (2021). Dendritic cell paucity in mismatch repair–proficient colorectal cancer liver metastases limits immune checkpoint blockade efficacy. Proceedings of the National Academy of Sciences *118*, 2105323118. https://doi.org/10.1073/pnas.2105323118.
26. Hegde, S., Krisnawan, V.E., Herzog, B.H., Zuo, C., Breden, M.A., Knolhoff, B.L., Hogg, G.D., Tang, J.P., Baer, J.M., Mpoy, C., et al. (2020). Dendritic Cell Paucity Leads to Dysfunctional Immune Surveillance in Pancreatic Cancer. Cancer Cell *37*, 289-307.e9. https://doi.org/10.1016/j.ccell.2020.02.008.
27. Mlecnik, B., Bindea, G., Angell, H.K., Maby, P., Angelova, M., Tougeron, D., Church, S.E., Lafontaine, L., Fischer, M., Fredriksen, T., et al. (2016). Integrative Analyses of Colorectal Cancer Show Immunoscore Is a Stronger Predictor of Patient Survival Than Microsatellite Instability. Immunity *44*, 698–711. https://doi.org/10.1016/j.immuni.2016.02.025.
28. Pelka, K., Hofree, M., Chen, J.H., Sarkizova, S., Pirl, J.D., Jorgji, V., Bejnood, A., Dionne, D., Ge, W.H., Xu, K.H., et al. (2021). Spatially organized multicellular immune hubs in human colorectal cancer. Cell *184*, 4734-4752.e20. https://doi.org/10.1016/j.cell.2021.08.003.

29. Liu, Y., Zhang, Q., Xing, B., Luo, N., Gao, R., Yu, K., Hu, X., Bu, Z., Peng, J., Ren, X., et al. (2022). Immune phenotypic linkage between colorectal cancer and liver metastasis. Cancer Cell, 1–14. https://doi.org/10.1016/j.ccell.2022.02.013.
30. Sathe, A., Mason, K., Grimes, S.M., Zhou, Z., Lau, B.T., Bai, X., Su, A., Tan, X., Lee, H., Suarez, C.J., et al. (2023). Colorectal Cancer Metastases in the Liver Establish Immunosuppressive Spatial Networking between Tumor-Associated *SPP1* + Macrophages and Fibroblasts. Clinical Cancer Research *29*, 244–260. https://doi.org/10.1158/1078-0432.CCR-22-2041.
31. Galetto, A., Buttiglieri, S., Forno, S., Moro, F., Mussa, A., and Matera, L. (2003). Drug-and cell-mediated antitumor cytotoxicities modulate cross-presentation of tumor antigens by myeloid dendritic cells. https://doi.org/10.1097/01.cad.0000097711.69687.64.
32. Galluzzi, L., Humeau, J., Buqué, A., Zitvogel, L., and Kroemer, G. (2020). Immunostimulation with chemotherapy in the era of immune checkpoint inhibitors. Nat Rev Clin Oncol *17*, 725–741. https://doi.org/10.1038/s41571-020-0413-z.
33. Bracci, L., Schiavoni, G., Sistigu, A., and Belardelli, F. (2014). Immune-based mechanisms of cytotoxic chemotherapy: Implications for the design of novel and rationale-based combined treatments against cancer. Cell Death Differ *21*, 15–25. https://doi.org/10.1038/cdd.2013.67.
34. Zhou, X., Yu, S., Zhao, D.-M., Harty, J.T., Badovinac, V.P., and Xue, H.-H. (2010). Differentiation and Persistence of Memory CD8+ T Cells Depend on T Cell Factor 1. Immunity *33*, 229–240. https://doi.org/10.1016/j.immuni.2010.08.002.
35. Chen, Z., Ji, Z., Ngiow, S.F., Manne, S., Cai, Z., Huang, A.C., Johnson, J., Staupe, R.P., Bengsch, B., Xu, C., et al. (2019). TCF-1-Centered Transcriptional Network Drives an Effector versus Exhausted CD8 T Cell-Fate Decision. Immunity *51*, 840-855.e5. https://doi.org/10.1016/j.immuni.2019.09.013.
36. Shum, E.Y., Walczak, E.M., Chang, C., and Christina Fan, H. (2019). Quantitation of mRNA Transcripts and Proteins Using the BD Rhapsody^{TM} Single-Cell Analysis System. Adv Exp Med Biol *1129*, 63–79. https://doi.org/10.1007/978-981-13-6037-4_5.
37. Aibar, S., González-Blas, C.B., Moerman, T., Huynh-Thu, V.A., Imrichova, H., Hulselmans, G., Rambow, F., Marine, J.-C., Geurts, P., Aerts, J., et al. (2017). SCENIC: single-cell regulatory network inference and clustering. Nat Methods *14*, 1083–1086. https://doi.org/10.1038/nmeth.4463.
38. Künzli, M., and Masopust, D. (2023). CD4+ T cell memory. Nat Immunol *24*, 903–914. https://doi.org/10.1038/s41590-023-01510-4.
39. Mair, F., Erickson, J.R., Frutoso, M., Konecny, A.J., Greene, E., Voillet, V., Maurice, N.J., Rongvaux, A., Dixon, D., Barber, B., et al. (2022). Extricating human tumour immune alterations from tissue inflammation. Nature *605*, 728–735. https://doi.org/10.1038/s41586-022-04718-w.
40. Plitas, G., Konopacki, C., Wu, K., Bos, P.D., Morrow, M., Putintseva, E. V., Chudakov, D.M., and Rudensky, A.Y. (2016). Regulatory T Cells Exhibit Distinct Features in Human Breast Cancer. Immunity *45*, 1122–1134. https://doi.org/10.1016/j.immuni.2016.10.032.

41. Korsunsky, I., Millard, N., Fan, J., Slowikowski, K., Zhang, F., Wei, K., Baglaenko, Y., Brenner, M., Loh, P. ru, and Raychaudhuri, S. (2019). Fast, sensitive and accurate integration of single-cell data with Harmony. Nat Methods *16*, 1289–1296. https://doi.org/10.1038/s41592-019-0619-0.
42. Che, L.H., Liu, J.W., Huo, J.P., Luo, R., Xu, R.M., He, C., Li, Y.Q., Zhou, A.J., Huang, P., Chen, Y.Y., et al. (2021). A single-cell atlas of liver metastases of colorectal cancer reveals reprogramming of the tumor microenvironment in response to preoperative chemotherapy. Cell Discov *7*. https://doi.org/10.1038/s41421-021-00312-y.
43. Wu, Y., Yang, S., Ma, J., Chen, Z., Song, G., Rao, D., Cheng, Y., Huang, S., Liu, Y., Jiang, S., et al. (2022). Spatiotemporal Immune Landscape of Colorectal Cancer Liver Metastasis at Single-Cell Level. Cancer Discov *12*, 134–153. https://doi.org/10.1158/2159-8290.CD-21-0316.
44. Meiser, P., Knolle, M.A., Hirschberger, A., de Almeida, G.P., Bayerl, F., Lacher, S., Pedde, A.-M., Flommersfeld, S., Hönninger, J., Stark, L., et al. (2023). A distinct stimulatory cDC1 subpopulation amplifies CD8+ T cell responses in tumors for protective anti-cancer immunity. Cancer Cell *41*, 1498-1515.e10. https://doi.org/10.1016/j.ccell.2023.06.008.
45. Di Pilato, M., Kfuri-Rubens, R., Pruessmann, J.N., Ozga, A.J., Messemaker, M., Cadilha, B.L., Sivakumar, R., Cianciaruso, C., Warner, R.D., Marangoni, F., et al. (2021). CXCR6 positions cytotoxic T cells to receive critical survival signals in the tumor microenvironment. Cell *184*, 4512-4530.e22. https://doi.org/10.1016/j.cell.2021.07.015.
46. Jansen, C.S., Prokhnevska, N., Master, V.A., Sanda, M.G., Carlisle, J.W., Bilen, M.A., Cardenas, M., Wilkinson, S., Lake, R., Sowalsky, A.G., et al. (2019). An intra-tumoral niche maintains and differentiates stem-like CD8 T cells. Nature *576*, 465–470. https://doi.org/10.1038/s41586-019-1836-5.
47. Gebhardt, T., Park, S.L., and Parish, I.A. (2023). Stem-like exhausted and memory CD8+ T cells in cancer. Preprint at Nature Research, https://doi.org/10.1038/s41568-023-00615-0 https://doi.org/10.1038/s41568-023-00615-0.
48. Rivest, F., Eroglu, D., Pelz, B., Kowal, J., Kehren, A., Navikas, V., Procopio, M.G., Bordignon, P., Pérès, E., Ammann, M., et al. (2023). Fully automated sequential immunofluorescence (seqIF) for hyperplex spatial proteomics. Sci Rep *13*, 1–14. https://doi.org/10.1038/s41598-023-43435-w.
49. Spitzer, M.H., Carmi, Y., Reticker-Flynn, N.E., Kwek, S.S., Madhireddy, D., Martins, M.M., Gherardini, P.F., Prestwood, T.R., Chabon, J., Bendall, S.C., et al. (2017). Systemic Immunity Is Required for Effective Cancer Immunotherapy. Cell *168*, 487-502.e15. https://doi.org/10.1016/j.cell.2016.12.022.
50. Kruse, B., Buzzai, A.C., Shridhar, N., Braun, A.D., Gellert, S., Knauth, K., Pozniak, J., Peters, J., Dittmann, P., Mengoni, M., et al. (2023). CD4+ T cell-induced inflammatory cell death controls immune-evasive tumours. Nature *618*. https://doi.org/10.1038/s41586-023-06199-x.
51. Ferris, S.T., Durai, V., Wu, R., Theisen, D.J., Ward, J.P., Bern, M.D., Davidson, J.T., Bagadia, P., Liu, T., Briseño, C.G., et al. (2020). cDC1 prime and are licensed by

1460 CD4+ T cells to induce anti-tumour immunity. Nature *584*, 624–629. https://doi.org/10.1038/s41586-020-2611-3.
52. Wu, R., Ohara, R.A., Jo, S., Liu, T.-T., Ferris, S.T., Ou, F., Kim, S., Theisen, D.J., Anderson, D.A., Wong, B.W., et al. (2022). Mechanisms of CD40-dependent cDC1 licensing beyond costimulation. Nat Immunol *23*, 1536–1550.
1465 https://doi.org/10.1038/s41590-022-01324-w.
53. Ahrends, T., Spanjaard, A., Pilzecker, B., Bąbała, N., Bovens, A., Xiao, Y., Jacobs, H., and Borst, J. (2017). CD4+ T Cell Help Confers a Cytotoxic T Cell Effector Program Including Coinhibitory Receptor Downregulation and Increased Tissue Invasiveness. Immunity *47*, 848-861.e5. https://doi.org/10.1016/j.immuni.2017.10.009.
1470 54. Lei, X., Khatri, I., de Wit, T., de Rink, I., Nieuwland, M., Kerkhoven, R., van Eenennaam, H., Sun, C., Garg, A.D., Borst, J., et al. (2023). CD4+ helper T cells endow cDC1 with cancer-impeding functions in the human tumor micro-environment. Nat Commun *14*, 217. https://doi.org/10.1038/s41467-022-35615-5.
55. Hoves, S., Ooi, C.-H., Wolter, C., Sade, H., Bissinger, S., Schmittnaegel, M., Ast, O.,
1475 Giusti, A.M., Wartha, K., Runza, V., et al. (2018). Rapid activation of tumor-associated macrophages boosts preexisting tumor immunity. Journal of Experimental Medicine *215*, 859–876. https://doi.org/10.1084/jem.20171440.
56. Garris, C.S., Wong, J.L., Ravetch, J. V, and Knorr, D.A. (2021). Dendritic cell targeting with Fc-enhanced CD40 antibody agonists induces durable antitumor
1480 immunity in humanized mouse models of bladder cancer.
57. Vonderheide, R.H. (2020). CD40 Agonist Antibodies in Cancer Immunotherapy. Annu Rev Med *71*, 47–58. https://doi.org/10.1146/annurev-med-062518-045435.
58. Zhang, L., Li, Z., Skrzypczynska, K.M., Fang, Q., Zhang, W., O'Brien, S.A., He, Y., Wang, L., Zhang, Q., Kim, A., et al. (2020). Single-Cell Analyses Inform Mechanisms
1485 of Myeloid-Targeted Therapies in Colon Cancer. Cell *181*, 442-459.e29. https://doi.org/10.1016/j.cell.2020.03.048.
59. Beatty, G.L., Chiorean, E.G., Fishman, M.P., Saboury, B., Teitelbaum, U.R., Sun, W., Huhn, R.D., Song, W., Li, D., Sharp, L.L., et al. (2011). CD40 Agonists Alter Tumor Stroma and Show Efficacy Against Pancreatic Carcinoma in Mice and Humans.
1490 Science (1979) *331*, 1612–1616. https://doi.org/10.1126/science.1198443.
60. Long, K.B., Gladney, W.L., Tooker, G.M., Graham, K., Fraietta, J.A., and Beatty, G.L. (2016). IFNγ and CCL2 Cooperate to Redirect Tumor-Infiltrating Monocytes to Degrade Fibrosis and Enhance Chemotherapy Efficacy in Pancreatic Carcinoma. Cancer Discov *6*, 400–413. https://doi.org/10.1158/2159-8290.CD-15-1032.
1495 61. Byrne, K.T., and Vonderheide, R.H. (2016). CD40 Stimulation Obviates Innate Sensors and Drives T Cell Immunity in Cancer. Cell Rep *15*, 2719–2732. https://doi.org/10.1016/j.celrep.2016.05.058.
62. O'Hara, M.H., O'Reilly, E.M., Varadhachary, G., Wolff, R.A., Wainberg, Z.A., Ko, A.H., Fisher, G., Rahma, O., Lyman, J.P., Cabanski, C.R., et al. (2021). CD40
1500 agonistic monoclonal antibody APX005M (sotigalimab) and chemotherapy, with or without nivolumab, for the treatment of metastatic pancreatic adenocarcinoma: an open-label, multicentre, phase 1b study. Lancet Oncol *22*, 118–131. https://doi.org/10.1016/S1470-2045(20)30532-5.

63. Byrne, K.T., Betts, C.B., Mick, R., Sivagnanam, S., Bajor, D.L., Laheru, D.A., Chiorean, E.G., O'Hara, M.H., Liudahl, S.M., Newcomb, C., et al. (2021). Neoadjuvant selicrelumab, an agonist CD40 antibody, induces changes in the tumor microenvironment in patients with resectable pancreatic cancer. Clinical Cancer Research *27*, 4574–4586. https://doi.org/10.1158/1078-0432.CCR-21-1047.
64. Vonderheide, R.H. (2018). The Immune Revolution: A Case for Priming, Not Checkpoint. Preprint at Cell Press, https://doi.org/10.1016/j.ccell.2018.03.008 https://doi.org/10.1016/j.ccell.2018.03.008.
65. Huang, Q., Wu, X., Wang, Z., Chen, X., Wang, L., Lu, Y., Xiong, D., Liu, Q., Tian, Y., Lin, H., et al. (2022). The primordial differentiation of tumor-specific memory CD8+ T cells as bona fide responders to PD-1/PD-L1 blockade in draining lymph nodes. Cell *185*, 4049-4066.e25. https://doi.org/10.1016/j.cell.2022.09.020.
66. Galletti, G., De Simone, G., Mazza, E.M.C., Puccio, S., Mezzanotte, C., Bi, T.M., Davydov, A.N., Metsger, M., Scamardella, E., Alvisi, G., et al. (2020). Two subsets of stem-like CD8+ memory T cell progenitors with distinct fate commitments in humans. Nat Immunol *21*, 1552–1562. https://doi.org/10.1038/s41590-020-0791-5.
67. Beltra, J.C., Manne, S., Abdel-Hakeem, M.S., Kurachi, M., Giles, J.R., Chen, Z., Casella, V., Ngiow, S.F., Khan, O., Huang, Y.J., et al. (2020). Developmental Relationships of Four Exhausted CD8+ T Cell Subsets Reveals Underlying Transcriptional and Epigenetic Landscape Control Mechanisms. Immunity *52*, 825-841.e8. https://doi.org/10.1016/j.immuni.2020.04.014.
68. Zhang, L., Yu, X., Zheng, L., Zhang, Y., Li, Y., Fang, Q., Gao, R., Kang, B., Zhang, Q., Huang, J.Y., et al. (2018). Lineage tracking reveals dynamic relationships of T cells in colorectal cancer. Nature *564*, 268–272. https://doi.org/10.1038/s41586-018-0694-x.
69. Zheng, C., Zheng, L., Yoo, J.K., Guo, H., Zhang, Y., Guo, X., Kang, B., Hu, R., Huang, J.Y., Zhang, Q., et al. (2017). Landscape of Infiltrating T Cells in Liver Cancer Revealed by Single-Cell Sequencing. Cell *169*, 1342-1356.e16. https://doi.org/10.1016/j.cell.2017.05.035.
70. Masuda, K., Kornberg, A., Miller, J., Lin, S., Suek, N., Botella, T., Secener, K.A., Bacarella, A.M., Cheng, L., Ingham, M., et al. (2022). Multiplexed single-cell analysis reveals prognostic and nonprognostic T cell types in human colorectal cancer. JCI Insight *7*. https://doi.org/10.1172/jci.insight.154646.
71. Prokhnevska, N., Cardenas, M.A., Valanparambil, R.M., Sobierajska, E., Barwick, B.G., Jansen, C., Reyes Moon, A., Gregorova, P., delBalzo, L., Greenwald, R., et al. (2022). CD8+ T cell activation in cancer comprises an initial activation phase in lymph nodes followed by effector differentiation within the tumor. Immunity *56*, 107-124.e5. https://doi.org/10.1016/j.immuni.2022.12.002.
72. Zhang, Y., Liu, G., Zeng, Q., Wu, W., Lei, K., Zhang, C., Tang, M., Zhang, Y., Xiang, X., Tan, L., et al. (2024). CCL19-producing fibroblasts promote tertiary lymphoid structure formation enhancing anti-tumor IgG response in colorectal cancer liver metastasis. Cancer Cell *42*, 1370-1385.e9. https://doi.org/10.1016/j.ccell.2024.07.006.
73. Espinosa-Carrasco, G., Chiu, E., Scrivo, A., Zumbo, P., Dave, A., Betel, D., Kang, S.W., Jang, H.-J., Hellmann, M.D., Burt, B.M., et al. (2024). Intratumoral immune

triads are required for immunotherapy-mediated elimination of solid tumors. Cancer Cell *42*, 1202-1216.e8. https://doi.org/10.1016/j.ccell.2024.05.025.
74. Magen, A., Hamon, P., Fiaschi, N., Soong, B.Y., Park, M.D., Mattiuz, R., Humblin, E., Troncoso, L., D'souza, D., Dawson, T., et al. (2023). Intratumoral dendritic cell–CD4+ T helper cell niches enable CD8+ T cell differentiation following PD-1 blockade in hepatocellular carcinoma. Nat Med *29*, 1389–1399. https://doi.org/10.1038/s41591-023-02345-0.
75. Qi, J., Sun, H., Zhang, Y., Wang, Z., Xun, Z., Li, Z., Ding, X., Bao, R., Hong, L., Jia, W., et al. (2022). Single-cell and spatial analysis reveal interaction of FAP+ fibroblasts and SPP1+ macrophages in colorectal cancer. Nat Commun *13*, 1742. https://doi.org/10.1038/s41467-022-29366-6.
76. Tauriello, D.V.F., Palomo-Ponce, S., Stork, D., Berenguer-Llergo, A., Badia-Ramentol, J., Iglesias, M., Sevillano, M., Ibiza, S., Cañellas, A., Hernando-Momblona, X., et al. (2018). TGFβ drives immune evasion in genetically reconstituted colon cancer metastasis. Nature *554*, 538–543. https://doi.org/10.1038/nature25492.
77. Cardenas, M.A., Prokhnevska, N., Sobierajska, E., Gregorova, P., Medina, C.B., Valanparambil, R.M., Greenwald, R., DelBalzo, L., Bilen, M.A., Joshi, S., et al. (2024). Differentiation fate of a stem-like CD4 T cell controls immunity to cancer. Nature. https://doi.org/10.1038/s41586-024-08076-7.
78. Binnewies, M., Mujal, A.M., Pollack, J.L., Combes, A.J., Hardison, E.A., Barry, K.C., Tsui, J., Ruhland, M.K., Kersten, K., Abushawish, M.A., et al. (2019). Unleashing Type-2 Dendritic Cells to Drive Protective Antitumor CD4+ T Cell Immunity. Cell *177*, 556-571.e16. https://doi.org/10.1016/j.cell.2019.02.005.
79. Tilsed, C.M., Principe, N., Kidman, J., Chin, W.L., Orozco Morales, M.L., Zemek, R.M., Chee, J., Islam, R., Fear, V.S., Forbes, C., et al. (2022). CD4+ T cells drive an inflammatory, TNF-α/IFN-rich tumor microenvironment responsive to chemotherapy. Cell Rep *41*, 111874. https://doi.org/10.1016/j.celrep.2022.111874.
80. Amgad, M., Stovgaard, E.S., Balslev, E., Thagaard, J., Chen, W., Dudgeon, S., Sharma, A., Kerner, J.K., Denkert, C., Yuan, Y., et al. (2020). Report on computational assessment of Tumor Infiltrating Lymphocytes from the International Immuno-Oncology Biomarker Working Group. Preprint at Nature Research, https://doi.org/10.1038/s41523-020-0154-2 https://doi.org/10.1038/s41523-020-0154-2.
81. Goldsborough, T., Philps, B., O'Callaghan, A., Inglis, F., Leplat, L., Filby, A., Bilen, H., and Bankhead, P. (2024). InstanSeg: an embedding-based instance segmentation algorithm optimized for accurate, efficient and portable cell segmentation. https://doi.org/doi.org/10.48550/arXiv.2408.15954.
82. Stuart, T., Butler, A., Hoffman, P., Hafemeister, C., Papalexi, E., Mauck, W.M., Hao, Y., Stoeckius, M., Smibert, P., and Satija, R. (2019). Comprehensive Integration of Single-Cell Data. Cell *177*, 1888-1902.e21. https://doi.org/10.1016/j.cell.2019.05.031.
83. Hao, Y., Hao, S., Andersen-Nissen, E., Mauck, W.M., Zheng, S., Butler, A., Lee, M.J., Wilk, A.J., Darby, C., Zager, M., et al. (2021). Integrated analysis of multimodal single-cell data. Cell *184*, 3573-3587.e29. https://doi.org/10.1016/j.cell.2021.04.048.
84. Kumar, B. V., Ma, W., Miron, M., Granot, T., Guyer, R.S., Carpenter, D.J., Senda, T., Sun, X., Ho, S.H., Lerner, H., et al. (2017). Human Tissue-Resident Memory T Cells

Are Defined by Core Transcriptional and Functional Signatures in Lymphoid and Mucosal Sites. Cell Rep *20*, 2921–2934. https://doi.org/10.1016/j.celrep.2017.08.078.
85. Jerby-Arnon, L., Shah, P., Cuoco, M.S., Rodman, C., Su, M.J., Melms, J.C., Leeson, R., Kanodia, A., Mei, S., Lin, J.R., et al. (2018). A Cancer Cell Program Promotes T Cell Exclusion and Resistance to Checkpoint Blockade. Cell *175*, 984-997.e24. https://doi.org/10.1016/j.cell.2018.09.006.
86. Borcherding, N.Y.Q.& S.K. (2024). scRepertoire v2: A toolkit for single-cell immune receptor profiling.
87. Andreatta, M., Tjitropranoto, A., Sherman, Z., Kelly, M.C., Ciucci, T., and Carmona, S.J. (2022). A CD4+ T cell reference map delineates subtype-specific adaptation during acute and chronic viral infections. Elife *11*. https://doi.org/10.7554/elife.76339.
88. Pedersen, C.B., Dam, S.H., Barnkob, M.B., Leipold, M.D., Purroy, N., Rassenti, L.Z., Kipps, T.J., Nguyen, J., Lederer, J.A., Gohil, S.H., et al. (2022). cyCombine allows for robust integration of single-cell cytometry datasets within and across technologies. Nat Commun *13*. https://doi.org/10.1038/s41467-022-29383-5.
89. Nirmal, A.J., and Sorger, P.K. (2024). SCIMAP: A Python Toolkit for Integrated Spatial Analysis of Multiplexed Imaging Data. J Open Source Softw *9*, 6604. https://doi.org/10.21105/joss.06604.